2015

Laser Guide Star Design Project for the USAF John Bryan State Park Quad Axis Observatory

Nathan Michael Figlewski
Wright State University

Repository Citation

Figlewski, Nathan Michael, "Laser Guide Star Design Project for the USAF John Bryan State Park Quad Axis Observatory" (2015). *Browse all Theses and Dissertations*. 2039.
https://corescholar.libraries.wright.edu/etd_all/2039

Laser Guide Star Design Project for the USAF John Bryan State Park Quad Axis Observatory

A thesis submitted in partial fulfillment of the
the requirements for the degree of
Master of Science

By

Nathan M Figlewski
B.S. in Physics, The Citadel, The Military College of South Carolina, 2012

2015
Wright State University
Graduate School

January 18, 2016

I HEREBY RECOMMEND THAT THE THESIS PREPARED UNDER MY SUPERVISION BY Nathan Figlewski ENTITLED Laser Guide Star Design Project for the USAF John Bryan State Park Quad Axis Observatory BE ACCEPTED IN PARTIAL FULFILLMENT OF THE REQUIREMENTS FOR THE DEGREE OF Master of Science.

Douglas T. Petkie, Ph.D.
Thesis Director

Douglas T. Petkie, Ph.D.
Chair, Department of Physics

Committee on
Final Examination

Douglas T. Petkie, Ph.D.

Elizabeth Beecher, Ph.D.

Tamara Payne, Ph.D.

Robert E. W. Fyffe, Ph.D.
Vice President for Research and
Dean of the Graduate School

ABSTRACT

Figlewski, Nathan Michael. M.S. Department of Physics, Wright State University, 2015.
Laser Guide Star Design Project for the USAF John Bryan State Park Quad Axis Observatory.

Atmospheric Turbulence has long remained one of the great unsolved problems in physics. Laser guide stars were invented in order for telescopes to overcome atmospheric turbulence while used in combination with adaptive optics. This study focuses on the design and implementation phase of a Rayleigh laser guide star for the John Bryan State Park Observatory, owned and operated by the United States Air Force. Atmospheric simulations, as well as optical modelling of proposed equipment, were completed to optimize the design of this laser guide star. In addition, a novel method for the implementation of the guide star onto this very unique four axis telescope platform is presented.

Table of Contents

List of Figures

List of Tables

I. **Introduction and Motivation**

Atmospheric sciences are of great interest to many fields of study, as the effects of the Earth's atmosphere have broad impacts. The effect of clear air turbulence on optical propagation is chief among the areas of study for optimizing electro-optic remote sensing. A deeper understanding of atmospheric turbulence will support improvement of predictive analytic optical propagation models. This thesis examines preliminary design concepts for a laser beacon system that can be used to measure atmospheric turbulence at various altitudes.

The atmosphere not only effects telescopy and the observation of the cosmos, but also communication with satellites, the propagation of radar and optical signals alike, and other directed energy efforts. Atmospheric turbulence is ordinarily powerful enough to obscure almost all imagery taken for ground observation of satellites without some sort of compensation. Caused by variations of the index of refraction along the optical path of interest, the perturbations have been plaguing astronomers and optical physicists for centuries. Their motion seems random and unpredictable, and their magnitude can vary quite substantially in a matter of seconds.

The next chapter will explain the history of the study of turbulence and derive the equations that drive the current models describing atmospheric turbulence such as the Kolmogorov and Hufnagel-Valley models. The limitations of telescopes under the influence of turbulence and the solutions to mitigate those limitations will also be touched on.

Following the chapter on turbulence is an explanation of guide stars are. The inner workings of the technology and the methods behind adaptive optics and guide stars, both natural and artificial, will be discussed.

The specific case of the United States Air Force's Air Force Research Laboratory's John Bryan Park Observatory will be used as a design objective. The equipment proposed to build an artificial guide star will be described in detail along with the reasons for which they were chosen.

In chapter four, several simulation programs will be described and used to model the proposed design. The programs are High Energy Laser End to End Optical Simulator (HELEEOS), Laser Environmental Effects Definition Reference (LEEDR), and the Satellite Visualization and Signature Tool (SVST). These will be used to model the atmosphere above the John Bryan Observatory platform, as well as model the propagation of a laser guide star for use by the observatory. The results of the simulations include backscatter figures, profiles of the turbulence, and the outcomes of identical scenarios using different turbulence models, and will provide the backbone of discussion on the overall feasibility of the proposed design.

In the final chapter, future experiments such as sodium guide stars, a technique for creating turbulence profiles called dynamic range gating, and adding adaptive optics to the John Bryan Observatory will be suggested.

II. Turbulence

II.1 The Problem

As astronomy has moved forward, telescopes were built larger in order to collect more light. Greedy in their photon budgets, scientists have been increasing the size of their telescopes. This increase in size initially led to disappointing results: the stars were still twinkling, and planets were still fuzzy! The atmosphere was soon fingered to be the culprit.

> The first astronomer to appreciate the importance of atmospheric conditions on telescopic images was Christian Huygens, who, around 1656, was using an aerial telescope of 123-feet focal length, the small objective of which was mounted on a high pole. He noted that stars twinkled and that the edges of the Moon and planets trembled in the telescope, even when the atmosphere appeared calm and serene. So frequent were nights of poor seeing that Huygens warned observers against too hastily blaming their telescopes [1].

Small variations in temperature and pressure cause the index of refraction to vary enough such that the photons traveling millions of light-years to their telescopes (and later modern CCD cameras) were distorted in such a way that entire stars seem to waver in the cosmos. Sir Isaac Newton noted soon thereafter in his 1704 work *Opticks*:

> Long Telescopes may cause objects to appear brighter and larger than short ones can do, but they cannot be so formed as to take away that confusion of the Rays which arises from the Tremors of the Atmosphere. The only Remedy is a most serene and quite Air, such as may perhaps be found on the tops of the highest Mountains above the grosser Clouds [2].

Newton had discovered that the cause was these variations in the atmosphere, and not from the blooming dispersion effect he previously thought all optical mediums suffered. It is interesting to note that he had also deduced a truth that modern scientists now use to their advantage; placing their observatories high above sea level on mountain peaks, and even above the atmosphere itself.

II.2 Closer Observation

The first opportunity that scientists had to observe the wavefront errors that resulted from turbulence was Foucault's knife-edge test.

This technique not only reveals the location and magnitude of imperfections in the figure of a primary mirror, but it also allows random wavefront variations, such as those due to atmospheric turbulence, to be visualized [1].

Originally, the knife edge test was used in a laboratory to evaluate the quality of a mirror. A knife edge is place at the center of a telescopes primary focus, using a uniform point source of light. The knife edge allows the small variations in a mirror to be seen in the form of spatial brightness variation in the image. This test can be performed with a laboratory collimated source or with a distant bright star as the effect is the same with both. In the case of using a star, the aberrations visualized are caused by a combination of the mirror errors and the atmosphere manipulating the wavefront, and thus causing a test result of variation of the brightness.

> The two sources of wavefront error can be separated by photography. Using short exposures of 1/20 second or less, photographs of the primary mirror made with a knife-edge show the combination of the figure errors and atmospheric turbulence patterns. With long exposures of tens of seconds, the rapidly changing turbulence errors average out, revealing only the imperfections in the figure of the mirror [1].

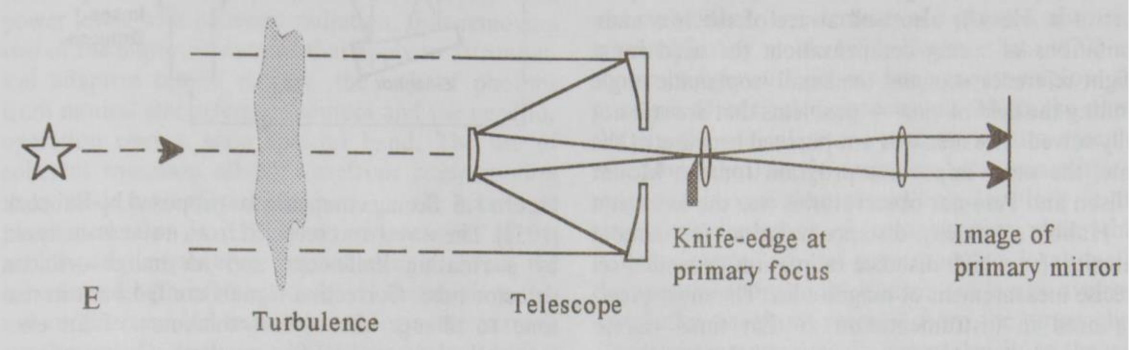

Figure 2.1 – A representation of the knife-edge test as used to observe atmospheric turbulence [1].

The knife edge test served as one of the first modalities for quantifying the effect of the atmosphere on astronomical observations.

Later, in 1900, Johannes Franz Hartmann describes his test that involved a mask with various holes over the aperture. Images of the resulting ray bundles were produced with photographic plates on either side of the focal plane, resulting in a matrix of spots. The spots could then have their positions measured as a function of time, the imperfections in the mirror could then be calculated from the displacement of the rays versus the pattern from perfect optics. The automation and increase of sophistication of this test lead to the Shack-Hartmann wavefront sensor, which is used in the study of turbulence and most, if not all, adaptive optics systems today [3].

The first Shack-Hartmann wavefront sensor (WFS) was a project for the United States Air Force for use in satellite image optimization. The observation of satellites is of great interest to the United States Air Force. Material analysis, functional characterization of assets in orbit, as well as tracking orbits are quite important to a concept called Space Situational Awareness (SSA). The better the imagery or photometry data, the more precisely observers can understand these sorts of characteristics. These methods can also be translated directly to astronomy and solar system exploration, as material analysis of asteroids and moons has been an area of study for quite some time. The experiment called for an array of lenses less than one millimeter in diameter and with a focal length of between 100 and 150 millimeters.

> The Air Force project was simulated in the laboratory. The target was a scaled photograph of a satellite using the correct angle of illumination. A 35-mm reflex camera was used to record the focused spots from the lens array. The focused

> patterns were low-resolution images of the satellite and not just spots. All images were identical so this did not affect the ability to determine centroids of the images. Atmospheric aberrations were simulated with a static phase plate. A pinhole was later used for a test target. …Accuracy was determined by a tolerance analysis and by comparing the measured results of an aberration plate, using the Shack-Hartmann sensor, to the measured results of a commercial Zygo interferometer. Accuracy was determined to be at least λ/20 [3].

The centroids for each image in the array was found, and then the movement of the centroids over time was measured. From these data, the experimenters were able to build a graphical representation of the time varying wavefront tilt vectors, allowing for a very high fidelity method of measuring both the direction and magnitude of wavefront manipulation [3].

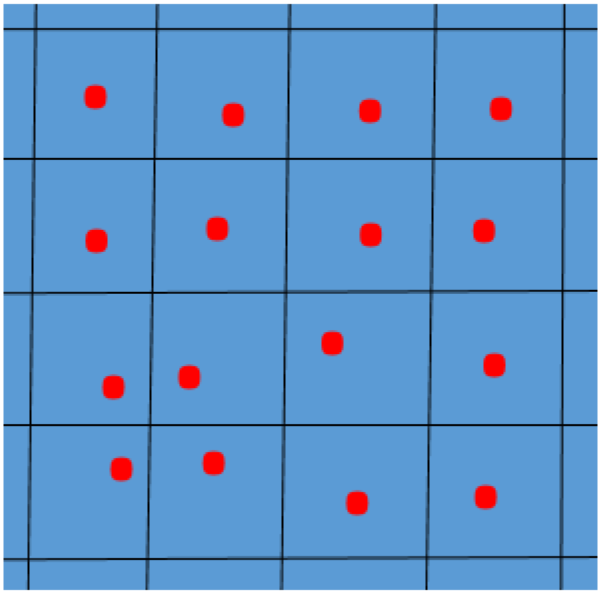

Figure 2.2: An example of a Shack-Hartmann WFS detector plane. In the absence of turbulence, the red dots would be in the center of their boxes, staying motionless with time. The dot distance from the square center can be used to calculate the wavefront tilt vectors.

The resultant wavefront is calculated by the following equation [4]:

$$\nabla\phi(x,y) = \theta_x(x,y)\hat{\imath} + \theta_y(x,y)\hat{\jmath} \tag{1}$$

where the measurements of the centroid shifts are given by [4]

$$\theta_x = \frac{\delta\phi}{\delta x} \text{ and } \theta_y = \frac{\delta\phi}{\delta y} \tag{2}$$

Shack-Hartmann WFS give scientists a way to measure the turbulent effect the atmosphere has on optical signals.

II.3 Initial Model Efforts

As for the turbulent effect of the atmosphere, Andrey Kolmogorov is credited with the creation of the most credible fluid dynamics model to date. In 1941, he proposed his now famous model which was involved with the concept of eddies in the atmosphere. These eddies are whirlpools of air which consist of turbulent motion, and are described by scales. The turbulent medium is divided into regions, and these regions are defined by their eddies. Large eddies can contain smaller eddies, and so on and so forth. To quote Lewis Fry Richardson;

> Big whirls have little whirls
> that feed on their velocity,
> and little whirls have lesser whirls
> and so on to viscosity [5].

Large scale eddies, denoted by use of the subscript 'o' for outer scale, are large volumes of air that can be used to describe turbulent atmospheres. These air masses move as a single unit, and are comprised of smaller volumes themselves. The characteristic velocity, u_o, of these large scale eddies moving through the Earth-centric reference frame,

$$u_o = \frac{l_o}{\tau_o} \tag{3}$$

Where l_o is the characteristic length of the eddy, and τ_o is the time scale of the turbulence in seconds. The time scale is also known as the 'large scale eddy turnover time' and can be estimated by l_o/μ [6]. The turbulent kinetic energy is defined as the kinetic energy that is associated with an eddy. This is measured by finding the RMS of the eddy's fluctuations in velocity. The turbulent kinetic energy is defined as

$$k = \frac{1}{2}\left(\overline{u_1^2} + \overline{u_2^2} + \overline{u_3^2}\right) \tag{4}$$

where $\overline{u_1^2}, \overline{u_2^2},$ and $\overline{u_3^2}$ are the averaged turbulence normal stresses [8]. It is the turbulent kinetic energy that is transferred from the large eddies to the small eddies in the concept of the energy cascade.

The turbulent kinetic energy is related to the root mean square turbulence intensity factor u' as written [6]

$$u' = \sqrt{\frac{2k}{3}} \tag{5}$$

If it is assumed that the energy of the eddy is dissipated in time τ_o, it is approximately true that

$$l_o \propto \frac{k^{\frac{3}{2}}}{\varepsilon} \tag{6}$$

with ε defined as the energy dissipation rate [6]. Small scale eddies, *l*, are contained within the large scale eddies, and define the turbulent medium in finer detail. These two qualities are related to the Reynolds number, Re [1].

The Reynolds number is a quantifier without units which is used to describe the flow patterns. Higher Reynolds numbers describe more complex turbulent flows, and lower Reynolds numbers represent the less complex laminar flow. Reynolds numbers are a ratio of momentum to viscosity, given by [1]

$$Re = \frac{\rho \mathrm{v} l_o}{\mu} = \frac{\nu l_o}{\eta} \tag{7}$$

where ρ is the fluid density, *v* is the mean velocity, l_o is the large scale flow length, μ is the viscosity of the fluid, and $\eta(\mu, \rho) = \frac{\mu}{\rho}$ (8) is the kinematic viscosity. Figure 2.3 shows a simple example which shows how these numbers describe the atmosphere. Note that Reynolds numbers can vary greatly in magnitude, from 1 to infinity.

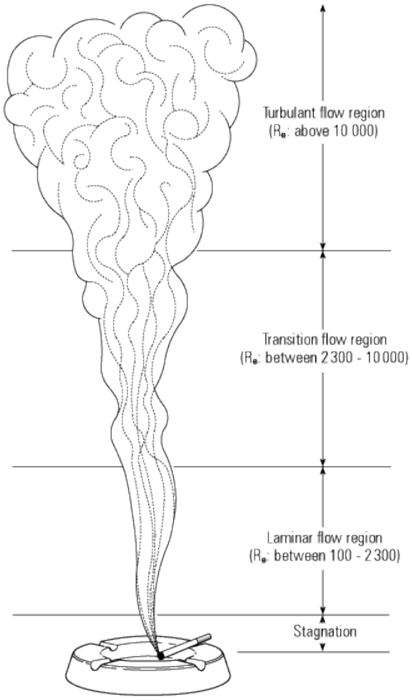

Figure 2.3: An illustration of Reynolds numbers and how they are used to describe turbulent flows [7].

Furthermore, we can now define a quantity called the turbulence Reynolds number, Re_l, as a function of k, l_o, and ν;

$$Re_l = \frac{k^{\frac{1}{2}} l_o}{\nu} \tag{9}$$

This quantity can be used to define the Reynolds number of all the eddy sizes, down to the magnitudes where the number is small enough to be considered a stable fluid. More than likely, numbers this small are describing molecular viscosity where the kinetic energy due to turbulence is released to the atmosphere in the form of heat. This transfer of energy scales as

$$\frac{{u_o}^2}{\tau_o} = \frac{u_o^3}{l_o} \tag{10}$$

as the eddies have an energy on the order of ${u_o}^2$ and a timescale of $\tau_o = l_o/u_o$.

Kolmogorov hypothesized that the large scale eddies had no directional bias on the smaller scales, or $l \ll l_o$. When the Reynolds numbers are above a certain limit, the small scales are considered isotropic. This is known as Kolmogorov's hypothesis of local isotropy. There is a critical scale, l_{cr}, that delineates between these large and small scales, such that [1]

$$l_o > l_{cr} > l \tag{11}$$

where values lying between $l_{cr} > l$ are isotropic.

Before moving on, it is important to introduce some other factors and concepts which play into the description of turbulence.

The first component to introduce is the turbulent kinetic energy dissipation factor, ε. This is the rate at which the kinetic energy is dispersed into the smaller eddies, and can be found via [9].

$$\epsilon = \nu \left[\langle \frac{\delta u_i}{\delta x_i} + \frac{\delta u_j}{\delta x_j} \rangle \langle \frac{\delta u_i}{\delta x_i} + \frac{\delta u_j}{\delta x_j} \rangle \right] \tag{12}$$

Given these two factors, we can use their relationships to find the length, velocity, and time scales of the turbulent eddies respectively [9]:

$$l_o = \left(\frac{\nu^3}{\varepsilon} \right)^{1/4} \tag{13}$$

$$u \ \ = (\nu\varepsilon)^{1/4} \tag{14}$$

$$\tau \ \ = \sqrt{\frac{\nu}{\varepsilon}} \tag{15}$$

The value l_o is one of the most important quantities in Kolmogorov theory known as the Kolmogorov length scale. This is the scale at which the turbulent kinetic energy is actually dissipated, as scales of length l_o (large scales) can be said to conserve their kinetic energy as a semi closed system. We can use the dissipation factor in combination with the Reynolds number to directly relate the large and small scales.

> For the process [of turbulence] to continue in a stable state, the rate of viscous dissipation must equal the rate of input turbulent energy. This condition implies that at any physical scale within the inertial range, the velocity fluctuations V are governed only by the scale size l and the rate of energy input and dissipation ε. Dimensional considerations then lead to the relationship
>
> $$V \propto \varepsilon^{1/3} l^{1/3} \qquad (16)$$
>
> which implies that the fluctuational energy in perturbations of size l is proportional to $l^{2/3}$. This is true for all scales within the inertial range. The size of the fluctuations depends only on the rate of energy input and dissipation ε. The relation between the inner scale $l_i$and the outer scale l_o is
>
> $$l \quad = \frac{l_o}{Re^{3/4}} \qquad (17)$$
>
> Thus, the greater the velocity of the flow, the larger is the Reynolds number and the smaller the inner-scale turbulence [1].

The term *inertial range* refers to the range between the large and small (Kolmogorov) scales such that $l_o > l_{cr} > l$. It is here that most of the turbulent energy is transferred to smaller scales rather than dissipated. Through the above relationship, the role of the turbulence Reynolds number in the description of eddy size is quite clear; the greater the flow velocity, the smaller the inner scale lengths become, Following this, it is natural to define the Kolmogorov power spectrum as a function of κ, the wave number; $\Phi = \Phi(\kappa)$ [1];

$$\Phi(\kappa)\mathrm{d\kappa} \propto \mathrm{V}^2 \propto \kappa^{-1/3} \tag{18}$$

The Fried coherence parameter, r_o, is a measure of turbulence strength that is useful to astronomers. It combines the refractive effects of the atmosphere in a single integrated value, and describes the maximum aperture size not dominated by turbulent effects. Strong turbulence corresponds to a small value for r_o, meaning that the diffraction limited aperture size is restricted significantly. Large r_o values represent weaker turbulence and larger diffraction limited collection aperture. Fried coherence parameters are defined as

$$r_o = [0.423k^2(\sec\xi)\int C_N^2(z)dz]^{-\left(\frac{3}{5}\right)} \tag{19}$$

where ξ is the zenith angle, and C_N^2 is the index of refraction structure constant, and k is the wavenumber [1].

II.4 Structure Functions

Another important tool for turbulence study is the structure function.

> The reasons for using these functions are discussed by Tatarski [1961] in his seminal book on wave propagation; they are summarized as follows. The mean values of many meteorological variables, such as temperature, pressure,

> and humidity, are continually changing over time scales of minutes to hours. These changes are relatively smooth but may represent large differences in the mean value of a variable. When these variables are analyzed, a problem arises in distinguishing changes in mean value from those changes due to slow fluctuations [1].

In reality temperature, pressure, and humidity are changing at a rate on the order of every 10^{-3} seconds due to the turbulence. Through the development of adaptive optics, scientists have found that the atmospheric changes which effect telescope iamgery happen at such a fast pace that a new brand of deformable mirrors had to be invented. First proposed by H. W. Babcock in 1953, modern deformable mirrors can correct wavefronts thousands of times per second [24]. This math is done via linear algebra, as normal analytical methods are simply too computationally expensive.

While local atmospheric variables change quickly, the overall background mean values also change slowly, too. To deal with this, we use the difference function from calculus, $F_t(\tau) = f(t+\tau) - f(t)$, where $f(t)$ is a non-stationary function, shows us that slow changes in *f(t)* have no effect on τ. Here, $f(t)$ is a function with a mean value which varies over time, and $f(t+\ \tau)$ is simply a translation in time.

Allowing this, $F_t(\tau)$ becomes a stationary function of time even though $f(t)$ is not. We are then able to define the structure function as

$$D_f(\tau) = \langle \left(f(t+\tau) - f(t)\right)^2 \rangle \tag{20}$$

so that $D_f(\tau)$ is a measure of fluctuation intensities of $f(t)$ over periods of time of magnitude of τ. More specifically in the case of turbulence, we assume a locally homogeneous and isotropic medium and use velocity components to construct a structure function

$$D_V(r) = \left|V(x) - V(x+r)\ \right|^2 = C_V^2 r^{\frac{2}{3}} \tag{21}$$

where C_V^2 is known as the velocity structure constant, and depends on the energy levels of the energy cascade [1]. Here, *r* is the propagation distance. In this example, *r* is the scale at which the turbulent kinetic energy is said to dissipate. Even in the presence of thermal equilibrium and absence of humidity, the potential for turbulence persists as turbulence is purely a result of the dynamic changes in the index of refraction.

> In Earth's atmosphere, temperature and humidity vary with altitude. Mechanical turbulence produces mixing of air from different altitudes, causing variations in temperature and humidity of similar scale to the underlying turbulence… A temperature structure function based on Kolmogorov's law may therefore be defined as follows
>
> $$D_T(r) = |T(x) - T(x+r)^2| = C_T^2 r^{\frac{2}{3}} \tag{22}$$
>
> where C_T^2 is the structure parameter for temperature variations [1].

One of the main causes in the fluctuation of the index of refraction is the change in density of the air, which is nominally caused by a change in temperature and/or pressure [10]. At any point, the index of refraction, N, can be approximated via the following [1]

$$N = (n-1)10^6 = \frac{77.6P}{T} \tag{23}$$

where P is pressure in millibars, and T is temperature in Kelvins [1]. A value for refractivity in a typical atmosphere is approximately 260. Changes in refractivity with respect to vertical propagation are mostly due to temperature changes

$$\delta N = -\frac{77.6P}{T}\delta T \tag{24}$$

and the index of refraction structure function becomes [1]

$$D_N(r) = C_N^2 r^{\frac{2}{3}} \tag{25}$$

with [1]

$$C_N^2 = \frac{\delta N}{\delta T} C_T \tag{26}$$

The factor C_N^2 is the index of refraction structure constant, and is used to gauge the strength of the turbulence in a given area. Values range from 10^{-17} $m^{-2/3}$ for weak turbulence and > 10^{-10} $m^{-2/3}$ for very strong turbulence. In the ‘very strong’ case, turbulence can be observed by the naked eye in the form of mirages, or the visual blurring seen on pavement on a hot summer day [11]. It should be noted that the actual wave bending, or mirror effect, on a hot day is an entirely different phenomenon, while the shimmering effect of this visual mirage is a result of turbulence. Often, temperature is used to calculate and record C_N^2.

Atmospheric turbulence is often measured by using temperature probes that determine the value of C_T^2. In terms of this parameter, the refractive index structure function is given by [1]

$$D_N(r) = \frac{78P}{T} C_T^2 r^{\frac{2}{3}} \qquad (27)$$

As a stochastic process, turbulence is described with an atmospheric power spectrum. A power spectrum is a three-dimensional equation which describes the atmospheric efficiency in relation to electromagnetic energy transportation. One of the more popular formulas for this is the Tatarski power spectrum [12];

$$\Phi_\mathrm{T}(\kappa) = \frac{\Gamma\left(\frac{8}{3}\right)\sin\left(\frac{\pi}{3}\right)}{4\pi^2} C_T^2 k^{-11/3} = 0.033 C_T^2 k^{-11/3} \qquad (28)$$

There is a critical value of k, known as $k_m = 5.92/l_o$, above which an assumption is made by the Tatarski method that there is a modifying term $e^{-\kappa^2/\kappa_m^2}$. This produces a drop off in the spectrum above κ_m. Also of note is $\Gamma\left(\frac{8}{3}\right)$, the gamma function [1].

This can also be applied to produce a power spectrum in terms of C_N^2. This yields the index of refraction power spectrum $\Phi_\mathrm{N}(\kappa) = 0.033 C_N^2 \kappa^{-11/3}$. Figure 2.4 shows an example of the Kolmogorov power spectrum.

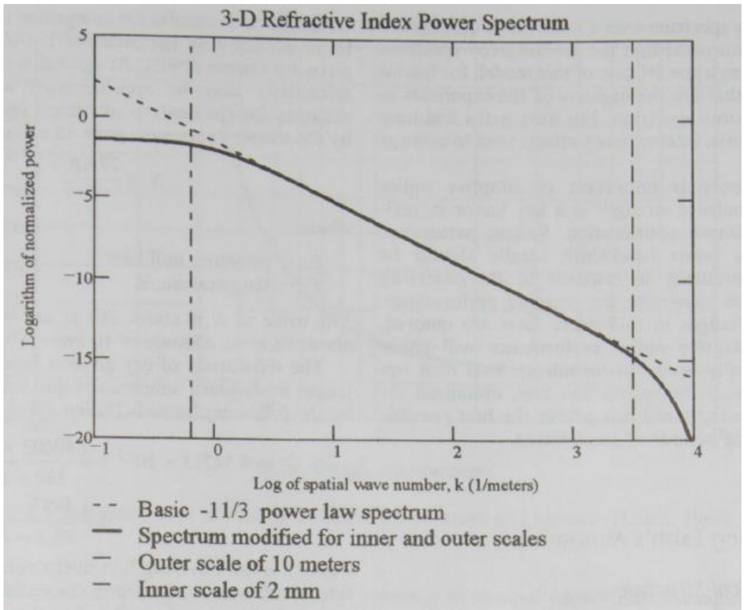

Figure 2.4: A atmospheric power spectrum based on the Kolmogorov model [1].

II.5 Atmospheric Structure

The structure of the Earth's atmosphere is divided into several parts. The troposphere extends from sea level to approximately 12 kilometers (km) in altitude, contains the bulk of the mass, and therefore contributes the most to turbulent effects. Above that, the stratosphere extends to approximately 50 km. The mesosphere begins at 50 km and stretches to 80 km, and is between the stratosphere and thermosphere, which begins at around 80 km and ends at 500 km. Since turbulence is negligible above 30 km, we will be most concerned with the troposphere [1].

The boundary layer of the Earth's atmosphere encompasses sea level to roughly one kilometer. It is here that most optical atmospheric modulation occurs. Geography, climate and weather, and time of day all greatly affect the magnitude of this modulation.

During the day, solar irradiation causes active convection,

> which may produce a factor-of-ten increase in the value of C_N^2 near the ground. Wyngaard et al. [1971] predicted that under these conditions the turbulence would follow an $h^{-4/3}$ [altitude] law, which has been confirmed by observations [1].

In astronomy, the term terminator is defined by the area of the earths surface where the surface is dark, but the sky is still illuminated by the sun. When an area is experiencing its terminator, the atmosphere is calmest, and the atmosphere comes closest to equilibrium. Somewhat surprisingly, due to radiative cooling of the Earth, the atmosphere again becomes more turbulent after sunset.

The planetary boundary layer occurs above the surface layer and extends to the order of eight to 12 km. Here, C_N^2 drops up to three orders of magnitude from what it is measured to be at sea level. It is in this boundary layer, however, that C_N^2 can vary by an order of magnitude within 200 meters [1]. Above the boundary layer is the tropopause, where turbulence can often spike due to wind shear. Finally, from the tropopause and higher, turbulence decreases quite substantially.

These layers all uniquely affect light that is traveling from the cosmos to a telescope, and their compounded effects are what we observe to be turbulence. Atmospheric scientists use the Fried coherence parameter, r_o, to describe the total wavefront distortion caused [13]. Different effects make up the total distortion: higher altitudes also introduce scintillation (or variations in intensity), beam wander, isoplanatic angle [1]. While r_o is a very useful parameter, it is plain to see that it does not accurately describe the distribution of turbulence as a function of altitude.

II.6 Atmospheric Modeling

Including the exosphere, which extends from 500 km upward, the Earth's atmosphere extends approximately 1,000 kilometers. Turbulence, however, comes into play only up until approximately 30 kilometers. Above that, the air lacks the density it requires to significantly affect the light which passes through it. The pressure at 30 kilometers is approximately 10 millibars, which is 1% of the pressure at sea-level. At the sodium layer, 90 km, atmospheric pressure drops to 10^{-6} that of sea-level. Refractivity, in equation (23), can also be described as a function of atmospheric density, and can be found via the following:

$$N(z,\lambda) = \left[8.3\times10^{-5} + \frac{2.4\times10\text{\textasciicircum}{-2}}{130-\lambda^{-2}} + \frac{1.6\times10^{-4}}{38.9-\lambda^{-2}}\right]\frac{\rho(z)}{\rho_s} \tag{29}$$

Here λ is the wavelength in microns, $\rho(z)$ is the atmospheric density at altitude z, and ρ_s is the standard atmospheric density, 0.001225 g/cm^{-3} at sea level. Sea-level refractivity, N_o, is about 280, while at 10 km it approaches 95 [1].

Wind plays an integral part in turbulence. Wind profiles generally take the ground wind speed, v_G, tropopause wind speed, v_T, the observational zenith angle ξ, and wind direction ϕ. What follows is the Greenwood wind profile model, which uses a Gaussian expression for its base [1].

$$v(z) = v_G + v_T e\left[-\frac{zcos(\xi)-H_T}{L_T}\right]^2 \times [\sin^2\phi + \cos^2\phi\cos^2\varsigma]^{\frac{1}{2}} \tag{30}$$

This model gives us a profile of the wind vector as a function of altitude, and allows for customization of the tropopause altitude, H_T.

> One of the most useful models is that of Hufnagel [1974], who proposed a heuristic model of the C_N^2 profile of the

> atmosphere for altitudes between 3 and 24 km, based on turbulence measurements made by many observers. [1]

With this model, Hufnagel discovered that the scintillation seen in stars is correlated with the instantaneous change in wind direction frequency, w^2, as

$$w^2 = \left(\frac{1}{15\ km}\right)\int_5^{25} v^2(h)\,dh \tag{31}$$

Here, $v^2(h)$ is the wind speed squared as a function of altitude. This w^2 factor is helpful for describing the strength of turbulence at higher altitudes. Hufnagel also developed a model for C_N^2 behavior as a function of altitude. This exponential function tracks C_N^2 values while taking into effect w^2 and the tropopause, falling rapidly once passing through it. It also includes the factor A which takes into account the fine structure of the turbulence as a function of time [13]:

$$C_N^2(h) = A\left[2.2\times 10^{-53}h^{10}\left(\frac{w}{27}\right)^2 e^{\frac{-h}{1000}} + 1\times 10^{-16}e^{\frac{-h}{1500}}\right] \tag{32}$$

and

$$A = e^{r(h,t)} \tag{33}$$

here r is some Gaussian (mean of zero) random variable. On average, most A values are approximately equal to e, or Euler's number [1]. This model fails below three km, where tropospheric winds are too widely variant to predict and a high majority of turbulence effects originate for ground based systems.

> To satisfy the needs of the defense community for the design of adaptive optics systems… Valley suggested the addition of a term for the surface layer turbulence [1].

To account for this in an updated model requested by the Department of Defense, the now famous Hufnagel-Valley (HV) turbulence model can be used [1].

$$C_N^2(h) = A\left[2.2\times 10^{-53}h^{10}\left(\frac{w}{27}\right)^2 e^{\frac{-h}{1000}} + 1\times 10^{-16}e^{\frac{-h}{1500}}\right] + Be^{\frac{-h}{100}} \tag{34}$$

Here B is now used to scale the surface turbulence term. This model has grown increasingly complex and detailed in the years since its development. Below, it is generalized to a series of exponential terms with are summed together [1]:

$$C_N^2(h) = Ae^{\frac{-h}{H_A}} + Be^{\frac{-h}{H_B}} + Ch^{10}e^{\frac{-h}{H_C}} + De^{\frac{-(h-H_D)}{2d^2}} \tag{35}$$

These models are used to predict highly accurate values for r_o (m) and seeing, θ_o (arc seconds). Table 2.1, taken from Hardy's Adaptive Optics for Astronomical Telescopes, is a concise look at different versions of this model and their constants. The two Mauna Kea (MK) models, 1 and 2 are to be used in the cases of very good and mediocre seeing respectively. Also, stellar imaging FWHM and θ_o are calculated using λ = 500 nm.

Model	A	H_A	B	H_B	C	H_C	D	H_D	*FWHM*	r_o	θ_o
	(E^{-15})	*(m)*	(E^{-17})	*(m)*	(E^{-53})	*(m)*	(E^{-16})	*(m)*	*(arc sec)*	*(m)*	*(arc sec)*
Hufnagel	0		27	1500	5.94	1000	0		1.15	0.11	1.1
HV 5-7	17	100	27	1500	3.59	1000	0		2.5	0.05	1.4
HV 10-10	4.5	100	9	1500	2.0	1000	0		1.26	0.10	2.1
HV 15-12	2	100	7	1500	1.54	1000	0		0.84	0.15	2.5
MK (1)	0		1	3000	1.63	1000	0		0.36	0.34	2.4
MK (2)	0		1	3000	1.63	1000	1	6500	0.53	0.24	1.9

Table 2.1: A concise glimpse of the constants different HV models use [1].

The data used for table 2.1 consists of 414 unique profiles that were collected over 20 nights in November 1987 and in June 1989 by Roddier el al [1990] using the University of Hawaii telescope.

The Tatarski model for C_N^2 is somewhat more complex than the Hufnagel-Valley model. It is a function of the temperature structure parameter, C_T^2 [13].

$$C_T^2 = \frac{4}{3k^{2/3}}\left(\frac{\bar{T}}{g}\right)^{2/3}\left(\overline{\omega'\theta'}\right)^{4/3} z^{-4/3} \tag{36}$$

Here, *k* is the von Karman constant, g is the acceleration of gravity, $\bar{T}$ is the mean temperature, $\overline{\omega'\theta'}$ is the covariance between the vertical velocity and temperature fluctuations, and *z* is the altitude in meters. This is then combined with a function of pressure and temperature, both as functions of altitude, to form [13]

$$C_N^2 = \left(79 \times 10^{-6}\frac{P}{T^2}\right)^2 C_T^2 \tag{37}$$

II.7 Anisoplanatism

Isoplanatism refers to the space over which wavefront errors are closely correlated. Thus, there is a limited area where the measurements and corrections of a distorted wavefront are useful. Anisoplanatism is the spatial decorrelation over an extended view. There are five flavors of anisoplanatism; aperture displacement, angular displacement, time delay displacement, focal displacement, and spectral displacement. For telescopes, angular anisoplanatism is caused by the turbulence distribution of the optical path. As can be expected, the further down the optical path length, the larger the effect of wavefront disturbance as the path length is exposed to more atmospheric turbulence. It is worthwhile to discuss a few equations that describe angular anisoplanatism. The first is the phase structure function as a function of path length [1].

$$D_\phi(r) = 2.914k^2(\sec\varsigma)r^{\frac{5}{3}}\int_{z1}^{z2} C_N^2(z)dz \tag{38}$$

Here, *r* is the separation between two points in the wavefront. Two beams which are coincident and observed to be separated by an angle *θ,* are truly separated by $r(z) = \theta z sec(\varsigma)$. The angular anisoplanatic error for any angle *θ* can be written as [1]

$$\langle\sigma_\theta^2\rangle = 2.914k^2(\sec\varsigma)^{8/3}\theta^{5/3}\int_{z1}^{z2} C_N^2(z)z^{\frac{5}{3}}dz = \left[\frac{\theta}{\theta_o}\right]^{\frac{5}{3}} \tag{39}$$

where the isoplanatic angle θ_o, makes use of the turbulence moment μ, to become [1]

$$\theta_o = \left[[2.914k^2\,(\sec\varsigma)^{\frac{8}{3}}\int_{z1}^{z2} C_N^2(z)z^{5/3}dz\right]^{-3/5} \tag{40}$$

This relationship can be extended to the Fried coherence parameter, r_o, via its definition. A ratio can then be made defining *h* as the mean height of the dominant turbulent layer [1]:

$$\frac{\theta_o}{r_o} = \left[6.88(\sec\varsigma)^{\frac{5}{3}}\frac{\mu_{\frac{5}{3}}}{\mu_o}\right]^{-3/5} = \frac{6.88^{-\frac{3}{5}}}{(\sec\varsigma)\bar{h}}\ or\ \theta_o = \frac{0.314(\cos\varsigma)r_o}{\bar{h}} \tag{41}$$

III. Laser Guide Stars and the John Bryan Observatory

III.1 Adaptive Optics

The basic concept behind a guide star is to provide a reference point. This reference point serves as a plane wave generator against which to collect a representative wavefront. The differences between a plane wave and what is measured reveals the nature of the turbulence, allowing the appropriate corrections to be made.

Observing, measuring, and recording atmospheric effects on optical propagation is no easy task. Wavefront sensor development has been a priority since the beginning of atmospheric science, but only until recently in the last quarter of the 20th century has it taken off. Both direct and indirect wavefront sensing techniques have taken great strides in the last few decades. Indirect sensing takes place when the characteristics of a wavefront are inferred from measurements of intensity across the entire collection aperture at the image plane. Direct measurements decompose the pupil of the collection optics and measure the wavefront itself. A Shack-Hartmann WFS is a direct sensing method, while image sharpening is an example of an indirect method. Since a Shack-Hartmann will be used for the proposed concept, it will be the focus of this discussion.

Figure 3.1 depicts the engineering behind a Shack-Hartmann WFS. These sensors work on the principle of zonal sensing, where the wavefront slope is measured in each sub-aperture of the pupil [1]. Since there are several measurements being done simultaneously, an average wavefront tilt can be obtained for a beam. The distorted wavefront is focused by each lenslet, and the translation of each spot is a measureable effect. If using square sub-apertures, the distribution function for intensity on the detector plane can be found by the following [1]:

$$I(x,y) = I_o \left(\frac{\sin \frac{\pi d x}{\lambda z}}{\frac{\pi d x}{\lambda z}} \right)^2 \left(\frac{\sin \frac{\pi d y}{\lambda z}}{\frac{\pi d y}{\lambda z}} \right)^2 = I_o \left(\frac{\sin ax}{ax} \right)^2 \left(\frac{\sin ay}{ay} \right)^2 \quad (42)$$

where *d* is the aperture diameter, and λ is the wavelength.

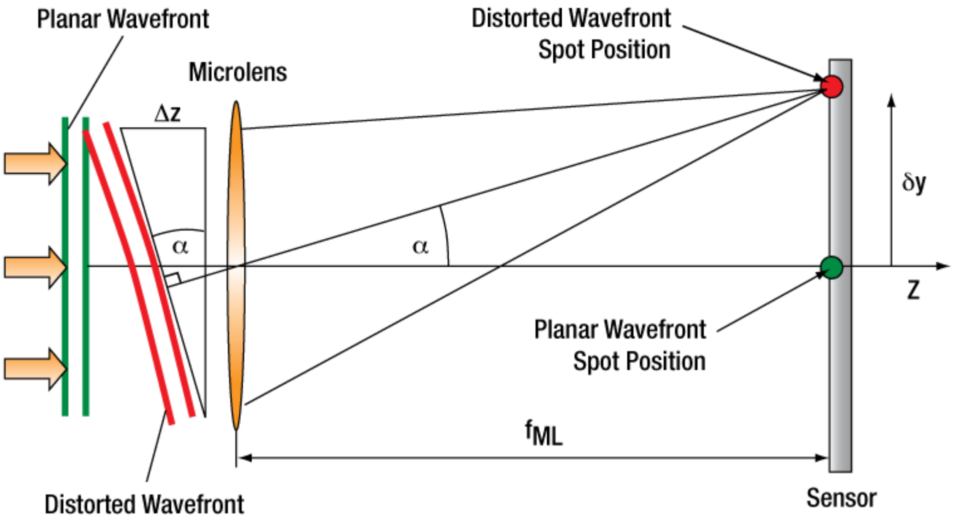

Figure 3.1: A close up illustration of the inner workings in the sub-aperture of a Shack-Hartmann WFS [14].

To combat the detrimental effects of a turbulent atmosphere on telescope observations, a method of real time wavefront corrections dubbed ‘adaptive optics’ was created. This method involves constantly measuring the incoming wavefront of a well-defined point source via a Shack-Hartmann WFS, and calculating the phase and amplitude difference from a plane wave. These values are then fed directly to a wavefront corrector, which modifies the incoming light in such a way that it corrects the wavefront and amplitude distribution that minimizes the atmospheric effects. There are two kinds of wavefront correctors; refractive and inertial [1].

Refractive wavefront correctors change the index or refraction of some optically translucent material, thus changing the optical path length. Refractive wavefront correctors are solid-state, using microelectronics to change the properties of the medium used [15]. Refractive correctors have the ability to provide micrometer spatial resolution [1]. Currently, the properties of liquid crystals are being investigated for use in this manner. For the time being, however, refractive correctors suffer from a relatively slow response time (on the order of milliseconds rather than microseconds) and thus are quite limited for use in adaptive optics [1]. Inertial wavefront correctors mechanically change the path length. There are some slight disadvantages to inertial correctors like spatial resolution (a mechanical limit). However, their mechanical nature allows for very fast response times.

The most popular form of inertial correctors is the deformable mirror. This is because it has a high dynamic range and can cover a wide range of the spectrum. There are two main types of deformable mirrors; continuous faceplate, and segmented mirrors. Continuous faceplate mirrors consist of multiple discrete actuators under a thin reflective membrane, which act independently of each other. Segmented deformable mirrors are are divided into multiple segments, with each having an actuator which can tilt its x-y plane. For telescopes, they are typically around 150 mm total in diameter, some with as many as 10,000 discrete segments separated by approximately 1 mm (another mechanical limit) [1].

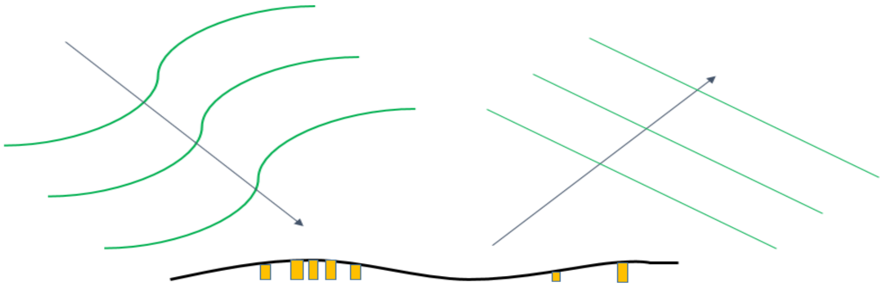

Figure 3.2: A deformable mirror corrects a turbulent wavefront to a plane wave.

Deformable mirrors are given wavefront data in the form of a matrix, where each element represents the corresponding *x* and *y* tilt needed to correct the wave front. This is done in real time at a frequency known as the Greenwood frequency, f_G. The Greenwood frequency is the minimum speed at which turbulence is influencing the wavefront, and as such is the speed at which it must be corrected. In reality, the correction speeds must be faster than the Greenwood frequency in order to account for actuation movement time. The Greenwood frequency is calculated by the following equation [13]:

$$f_G = 2.31\lambda^{-\frac{6}{5}}\left[sec\xi \oint C_N^2(z)v(z)^{\frac{5}{3}}dz\right]^{\frac{3}{5}} \tag{43}$$

Greenwood frequencies range from 10s of Hertz in weak turbulence to up to and above several kilohertz in cases of strong turbulence (thus the need for fast acting actuators). This process is very computationally intensive, as there is a great deal of linear algebra calculations that must be made at this frequency in order to properly correct the wavefront in real time. Powered with this mathematics, the next step is to create a reference point in the sky with which to calculate the differences, leading to the development of guide stars.

III.2 Natural and Artificial Guide Stars

A guide star is a slight misnomer as they are not guiding in the original sense of the word. The original “guide” stars were natural; stars that were bright enough point sources that they could be reliably used as a reference for wavefront distortion measurement. Since the light is spread over many lenslets in the Shack-Hartmann wavefront sensor, these requirements set quite a high bar and, naturally, few stars met the qualifications. A solution would take the form of artificial guide stars created by lasers. These artificial guide stars, known as laser guide stars, allow much more versatility for astronomers, giving them the ability to create a reference point wherever one is needed. There are two types: Rayleigh and sodium laser guide stars.

The more recent generation of guide star, Sodium guide stars, make use of the sodium layer in the mesosphere, approximately 90 kilometers above mean sea level. This sodium is theorized to be created by meteorites burning up in the atmosphere. These guide stars utilize a continuous wave (CW) laser tuned precisely to 589.1 nanometers (nm) [1]. This wavelength matches the resonance frequency of sodium and is absorbed by sodium atoms present at this layer spontaneously. Photons are created as a result of the energy level change in the electron state.

The first artificial guide stars, Rayleigh guide stars, take advantage of Rayleigh scattering effects in the lower atmosphere. Rayleigh scattering is the result of light interacting with particles whose size is smaller than the wavelength. These molecular or atomic ‘scatterers’ become like a radiating dipole which is charged by the incoming light, causing it to move at the same frequency and become an emitter.

Rayleigh guide stars can only be created much lower in the atmosphere, because the scattering is dependent on molecular density. This allows for studying characteristics of the main turbulence generating layer. The wavelength chosen by most is the green line, 532 nm, because as will be shown, this scatters in the atmosphere very efficiently. The availability of relatively cheap solid state lasers also makes this an attractive option. Some variants of Rayleigh guide stars use gas lasers and utilize the ultra-violent wavelengths around 355 nm [16].

There are certain considerations when choosing a laser to be used as an artificial guide star. For a Rayleigh guide star, the lasers pulse rate should be approximately ten times faster than the Greenwood frequency in order to provide sufficient continuous wavefront correction [13]. Obviously, the installation of a laser greatly effects the telescopes optics, requiring additional components to allow the laser to share the same optical path. Furthermore, unwanted scattered light must be rejected from the science images as well as the adaptive optics systems.

The equation which drives the efficiency and efficacy of laser guide stars is the lidar equation. This equation gives us the number of expected photon detections based on a range interval Δz.

$$N(z) = \left(\frac{E\lambda}{hc}\right)(\sigma_B n(z)\Delta z)\left(\frac{A_R}{4\pi z^2}\right)(T_o T_A^2 \eta) + N_B \tag{44}$$

Here, the equation has been broken into four discreet sections: probability of scattering, probability of photon collection, probability of photon detection, and the background noise [1].

The first term, called the transmitted pulse energy due to the encapsulation of total laser energy leaving the beam house, contains the laser's pulse energy, E, the wavelength, λ, Planck's constant, h, and finally c is the speed of light. The second term, scattering probability contains the backscatter cross-section σ_B, the number density of scatterers at range z $n(z)$, and the range gate length Δz. The number density of scatterers is defined as the number of air particles per meter cubed at range z. The photon collection capability is driven by the detector's receiving area A_R, and limited by the square of the distance to the center of the range gate z^2. The detection probability is a function of the transmission of the transmit and collection optics T_o, the one way transmission of the atmosphere from the guide star down to the telescope T_A, and the quantum efficiency of the detector η, at the specified wavelength λ. Finally, the background noise N_B, is added [1].

Since our primary focus is atmospheric studies, we proposed a Rayleigh guide star for the John Bryan Observatory Quad-Axis Telescope to take advantage of Rayleigh scattering to create the beacon. The Rayleigh backscatter cross-section is therefore used in the lidar equation, and is defined as

$$\sigma_B^R = \frac{\pi^2 \left(n^2 - 1\right)^2}{N^2 \lambda^4} \tag{45}$$

Here, n^2 is the square of the index of refraction, and N^2 is squared atomic density of air [1]. Note the λ^{-4} dependence. This shows that the shorter the wavelength, the more successful the scattering and thus a more efficient beacon is made. Coincidently, this is why the sky appears blue.

A problem arises with scattering a laser beam in the lower atmosphere; there is no selective scattering. This means that we can't pick and choose the section of the atmosphere in which the beam scatters, but instead must sample a section of the beam while subtracting the rest. Range gating is a technique for excluding unwanted photons from being counted by calculating the time of flight. An electronic shutter in front of the detector rejects light at the same frequency and duration as the laser fires, effectively blocking all other photons but those emanating from the guide star. The frequency at which the detector is shuttered must be synched to the time it takes for the light to travel from the desired beacon altitude to the detector plane. The range gate frequency, f_z is related to the time of flight, t_f, and the laser's repetition rate, *f*. Time of flight relies on *z*, the range to the middle of the scatter volume.

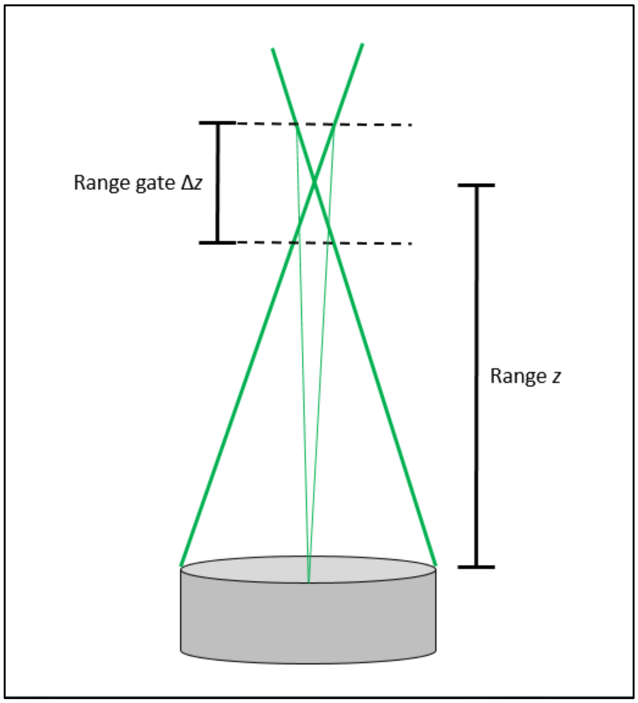

Figure 3.3: A Rayleigh laser guide star. The entire guide star, or beacon, is comprised of the volume encompassed in the range gate. All other scattered light is rejected by the detector's electronic shutter.

$$t_f = \frac{2z}{c} \tag{46}$$

Figure 3.3 depicts the structure of a Rayleigh laser guide star. The range gate size, Δz, in combination with laser pulse width, is what will drive the rejection shutter speed. The projection aperture, D_P, will be the primary telescope receiver aperture in this case. Some Rayleigh guide stars choose to have a bistatic approach to the laser launch system, but this can create unwanted problems with spot elongation as well as exacerbate the anisoplanatism challenges. In order to permit easy range gating, pulsed lasers are used for Rayleigh guide stars. The quick pulses disperse their energy into the atmosphere rapidly and the light from the chosen altitudes begins to travel back down via backscatter to the detector. The detector is then un-shuttered after time of flight and from the desired range gate, and then shuttered again very quickly. This process allows only the light from the chosen section of the scattered light to be measured.

The angular size of the guide star, $\Delta\alpha$, goes as $\Delta\alpha = 2.44\frac{\lambda}{d}$, where d is the smaller of either the subaperture size of the wavefront sensor or Fried coherence parameter [1]. This is identical to the equation for nominal laser beam divergence except for the addition of a 2.44 scaling factor. Sensors sub-aperture size can be substituted for the Fried coherence parameter in the case that $d > r_o$. To find the maximum range gate for a given guide star, the following can be used [1]:

$$\Delta z = \frac{2\Delta\alpha z^2 D_P}{[D_P^2 - (z\Delta\alpha)^2]} \tag{47}$$

This equation allows the user to minimize laser energy requirements and fine tune the efficiency of the artificial guide star. The maximum scatter length allows for the greatest amount of photons to be collected, while still avoiding the diffraction limit of the wavefront sensor sub-apertures.

III.3 John Bryan Observatory Quad Axis Telescope

The United States Air Force (USAF) Air Force Research Laboratory (AFRL) owns and operates a very unique asset located in John Bryan State Park outside of Dayton, Ohio. The specialized mount for this telescope has four axes, enabling high fidelity satellite tracking.

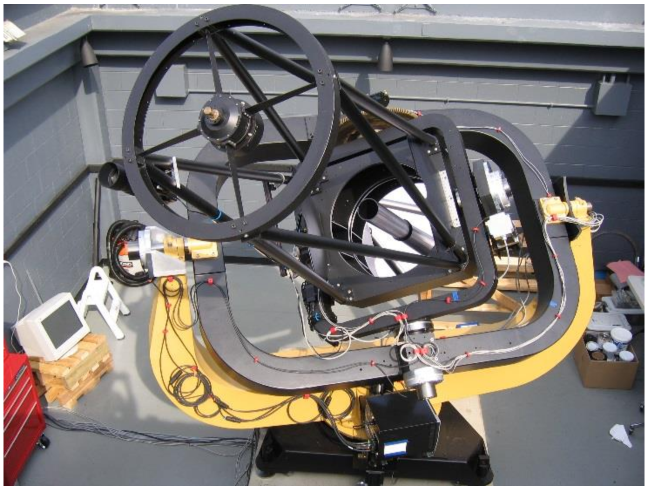

Figure 3.4: The John Bryan Observatory Quad-Axis Telescope (JBO-Q).

This telescope was designed and built by Kenneth E. Kissell in 1965, and returned to the USAF at John Bryan State Park in 2008 [17]. It has since been refurbished and given mechanically driven gears to be used for computer controlled auto-track. Software has been written to drive the four independent axes, and as of June 2014 has achieved a closed loop track of a satellite in low Earth orbit (LEO). The USAF is interested in turbulence research, as it relates to the propagation of laser communications, directed energy weapons, and space situational awareness. There also exists great curiosity for academic research in the area as was discussed in chapter one.

III.4 Laser Choice

Choosing a laser to be used in a guide star requires combing through the requirements that where mentioned in chapter two, in addition to a few others. The power requirements may be quite large, pulse widths must be short (but not too short), and beam quality is very important. Since Rayleigh guide stars require a laser pulse, there are two options: either a pulsed laser or a CW laser with transistor-transistor logic (TTL) modulation or a very high fidelity chopper wheel. TTL modulation electronically switches the laser on and off very quickly, while a chopper wheel physically blocks it at a set frequency. Both methods have a decent dynamic range, but they have a negative effect on pulse shape. Laser profiles with a sharp temporal edge, like what would be caused by these modulation methods, have distinct diffraction rings around the primary beam [18]. This is caused by Fraunhoffer diffraction, which is when a beam of light is partially blocked by an obstacle, in this case the laser beam port. Some of the light is scattered around the object, and light and dark bands are seen around the edge of the shadow. These rings can contain up to 16% of the total laser energy, degrading beam integrity before it leaves the laser launch telescope [13]. If the beam intensity is spatially tapered off, however, most of the energy is conserved in the beam structure rather than diffracted.

Gaussian beam profiles are described by a Gaussian distribution of laser energy out from the center of the beam. Because of the superior (for this application) beam shape, a Gaussian beam is preferred over the CW modulation methods. Gaussian beam profiles come in the form of the following equation [13]:

$$A(r) = A_o e^{-2\left(\frac{r}{\sigma}\right)^2} \tag{48}$$

Here, A_o is the maximum intensity value of the beam, r is the radial distance, and σ is the standard deviation of the beam spot size of the intensity values. Beam intensity is a function of total power, P, and beam waist w, and is defined as

$$I = \frac{2P}{\pi w^2} \tag{49}$$

$$\text{where } w(z) = w_o \left[1 + \left(\frac{\lambda z}{\pi w_o^2}\right)\right]^{1/2} \tag{50}$$

Here, w_o is the beam waist [1]. Switching the variables in the Gaussian distribution function for terms of irradiance, we get

$$I(r) = I_o e^{-2\left(\frac{r^2}{w^2}\right)} = \frac{2P}{\pi w_o^2} e^{-2\left(\frac{r^2}{w(z)^2}\right)} \tag{51}$$

TEM00 cavities project a Gaussian laser beam with this profile [13], [1]. This profile is preserved whether the beam is bent, expanded, concentrated, or otherwise directed, and it is for this reason Gaussian lasers are chosen for Rayleigh laser guide stars [19].

Wavelength is of great importance to laser guide stars, as there is a wavelength dependence on the Rayleigh backscatter cross-section. Since σ_B^R contains a λ^{-4} relationship, the pulse energy requirement depends directly on chosen wavelength. The trade space is small, but finite, so it should be investigated. For this study, three potential lasers were examined at three distinct bandwidths; ultraviolet (355 nm), visible (532 nm), and infrared (1064 nm or 1.064 micons). By varying the laser wavelength, the efficiency of each as a laser beacon can be determined and optimized. Additionally, water and other aerosols in the atmosphere both scatter and absorb each wavelength differently, giving a slightly varied turbulent profile [1].

Laser beam divergence must also be taken into consideration. A beam that diverges too much would be of poor quality for a laser beacon as the beam could not be properly focused. Thus, the measurement of beam divergence, or Θ, is of great significance. For a TEM00 mode laser, beam divergence in air can be calculated by the following equation [13]:

$$\Theta = \frac{4\lambda}{2\pi n w_o} = \frac{4\lambda}{2\pi w_o} \tag{52}$$

Here, w_o denotes the laser beam waist. The closer to zero (or a truly collimated beam), the more efficient the beam delivery and more useful the guide star.

Pulse width must be considered as many modern lasers have sub ten nanosecond (ns) pulses, with some pulses lasting picoseconds (ps). The return time of light from the beacon is on the order of 7 microseconds (μs), so the laser pulse must be significantly shorter than that in order for the return for each pulse to be collected separately. However, if the pulse is too short, there is not enough time for an effectively detectable scatter. The lasers chosen for these simulations all have pulse widths between 10 and 100 ns. Table A.1 contains more information about the lasers chosen for the simulations.

For this study, the Matrix 532-14 laser by Coherent will be the visible laser, the Questek 2580 Excimer Laser will be used for the ultraviolet, and a Spectra-Physics VGEN-QS will be used for the 1064 nm laser. These have all been chosen for their short pulse width, kilohertz repetition rate, energy output, and beam quality. Please see the appendix for laser specifications.

III.5 Beam Injection Optics

As was mentioned previously, there are a number of approaches for launching the laser into the sky to create an artificial guide star. Astronomers can use the full aperture of the telescopes collection optics (monostatic), or a co-aligned beam that is offset from the collection axis by some small distance (bistatic). Steering the beam into the launch optics can be accomplished through use of a Coudé path. Coudé paths allow the beam to be steered into the launch optics through the mechanical telescope mount itself [20]. The JBO-Q, unfortunately, does not have a Coudé path, and the costs of augmenting it to include one are prohibitive and would be a detriment to the performance of the telescope. As a result, further options were studied.

Fiber optics are an ever growing area of interest, as they offer mobility and efficient transport of light. With no Coudé path in the JBO-Q and due to its unique four axis movement, using traditional injection optics would be exceptionally complex. It is for this reason that fiber optics will be used to launch the laser guide star. Using fiber optics comes with a few concerns, however. Bending of fiber, although chief among its versatile qualities, lessens the efficiency of the energy transportation. The greater the angle of the bend, the greater the losses will be [21]. Another factor to consider is the damage threshold of the fiber itself. High power fiber optic patch cables are significantly more expensive than communications grade, but offer a much safer damage threshold [21]. In the interest of preserving the fiber further, a larger diameter fiber should be used. This allows for more energy to be distributed over a greater area, lessening the energy burden on the fiber optic material. For this study, a Photonic Crystal Fiber (PCF) endlessly single mode, large-mode-area-fiber optic cable with a damage threshold of 5 GW/cm^2 will be used, as can be purchased from Thorlabs (part number LMA-PM-5) for $157 per meter increment. The attenuation specifications for this fiber can be found in the appendix.

The laser itself, along with fiber injection equipment, will be located on an optical bench near the telescope pier mount. Upon exiting the beam house, the laser enters the fiber optics via a 1.5 inch diameter fiber collimator. This collimator focuses the beam down to the small fiber size, 15 µm. The fiber optic cable itself will actually be a fiber optic patch cable that includes an anti-reflective coating on the connector ends to decrease back-reflections, in turn increasing efficiency. This fiber cable will follow the cable path opposite the acquisition scope, and open the beam back up to free space via another fiber collimator near the edge of the truss. The acquisition scope is a smaller telescope mounted on the side of the main telescope.

III.6 Laser Launch

From the end of the fiber, the beam travels to a mirror located at the end of the truss which reflects the light into a laser launch telescope that is mounted on the back of the secondary mirror. This laser launch telescope will feature fine adjustable mirrors in order to co-align with the prime mirror.

The range gate used for this study will be a two kilometer long layer, nominally centered approximately 11 kilometers in altitude directly above the telescope. For the purposes of turbulence studies, the range gate might be adjusted to smaller intervals. The smaller the range gate, however, the less laser light will be returned. The LIDAR equation will be the primary function which drives the study, comparing the different lasers with multiple atmospheric models, and calculating the backscattered photons detected by a Thorlabs wavefront sensor (part number WFS20-5C).

This wavefront sensor has a detectable range beginning at 300 nm and extending to 1100 nm. There is a relative response curve included in the instruction manual, and this figure has been added to the appendix (see Figure A.2). The relative responsiveness peaks at approximately 500 nm, so the 532 nm laser will be the easiest to detect. It is also, however, the dimmest laser. The camera is also capable of an 880 Hz framerate, and has a shutter speed ranging from 5 µs to 88 ms, with a trigger accuracy of 5ns.

III.7 Precedence of Design

While this is the first time that such a laser injection method has been done on such an intricate and unique mount, it is not the first fiber optic laser guide star. The Subaru Observatory in Mauna Kea, Hawaii has utilized this system design since 2006.

While the Subaru telescope is much larger (the Subaru is 8.2 meters in diameter), and the guide star is a sodium guide star, a similar design would work well for the JBOQ [22].

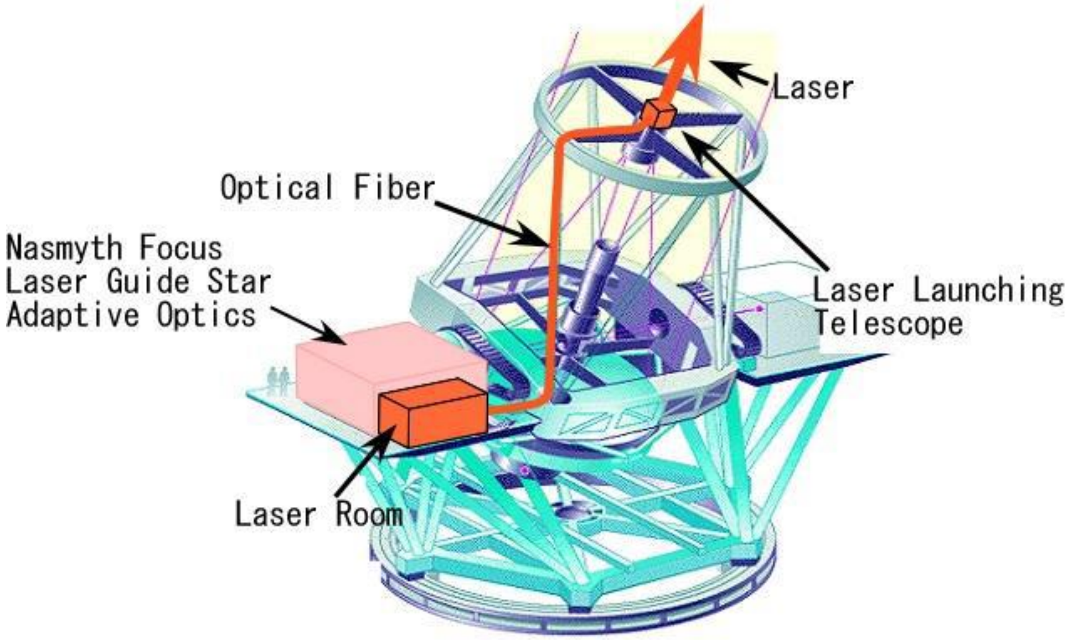

Figure 3.5: The Subaru Observatory's Sodium Laser Guide Star front end system [22].

The large scale nature of the Subaru Observatory allows them to have much more real estate than the 24" telescope at John Bryan State Park is permitted. Not quite so surprisingly, however, many of the design concepts transfer straightforwardly.

Like the planned laser bench section of the JBO-Q, the Subaru has a room specifically designed to house the laser. This is more along the lines of a traditional Coudé room, however, and is not quite possible within the constraints of this design. The Subaru Observatory also uses the same type of fiber optic cable, PCF, to transfer their laser from the beam conditioning area to the laser launch telescope. Finally, the laser launch telescope is directly on the back of the secondary mirror, which is precisely the plan for the JBO-Q. Based on the successful first light and subsequent use of the Subaru Observatory's sodium guide star, and the confidence that the proposed design will scale down to the smaller 24" JBO-Q, the probability of success is more than sufficient to press forward.

IV. Laser Propagation Simulations

The United States Air Force's graduate school, the Air Force Institute of Technology, has developed a number of atmospheric modelling programs for use in studying electromagnetic propagation. Most notably for optical methods, the High Energy Laser End to End Optical Simulator (HELEEOS) and the Laser Environmental Effects Definition and Reference (LEEDR) programs are used to model fully integrated laser systems, and model the effect of the atmosphere on the propagation of the laser.

First, using the lidar equation discussed in Chapter III as well as the atmospheric model discussed in Chapter II, a master lidar equation was created. This equation is a function of altitude, and the end result is power returned to the detector. This is accomplished by translating the photon per second counts into power. The result is a figure which details the power returns of each of the three lasers as a function of altitude.

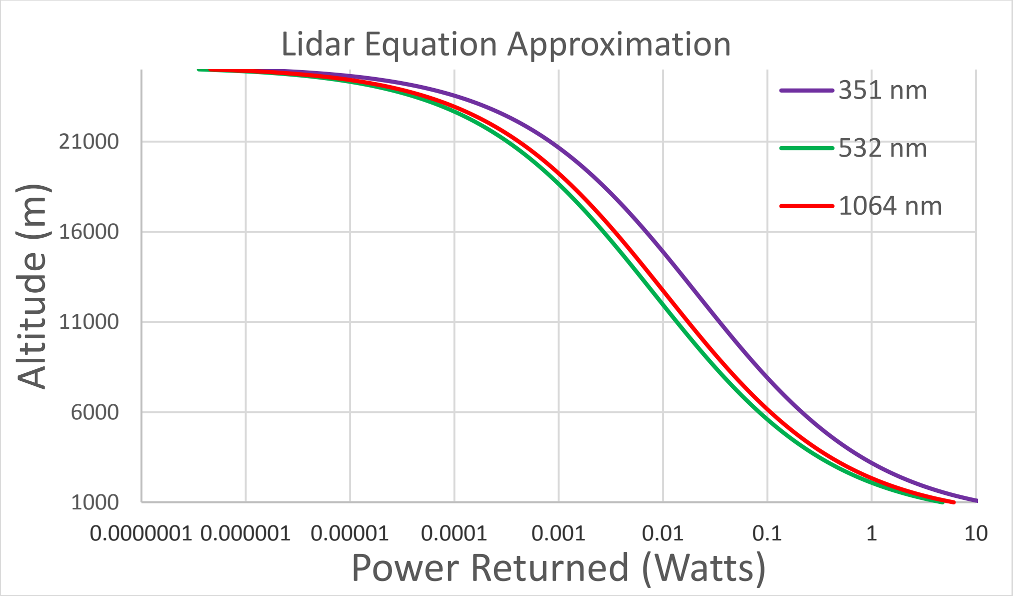

Figure 4.1: An approximation of the lidar equation as a function of altitude for each of the three laser wavelengths.

Note that this will be significantly less accurate than the other simulations to follow, but the results are analogously similar. The main cause of the differences is the accuracy of the atmospheric models. The lower fidelity model used as a first order approximation (Figure 4.1) yields less accurate results as the altitude increases because the overall model accuracy falls off. However, it will be seen that the relative differences between the three lasers stands true.

IV.1 High Energy Laser End to End Optical Simulator

HELEEOS allows for an all-inclusive look at the performance of a specified laser optical system. For this study, a Rayleigh laser guide star is modeled, and then the theoretical returned photons collected by the detector, in this case a wavefront sensor, are calculated. Thus, by entering the parameters specified by the chosen equipment, a comparison can be made of each proposed system in order to optimize the equipment.

In HELEEOS, the user has the option to choose a platform, which will be the laser launch system described above. The program allows for the total optical effects of the designed system to be entered and calculated in a complete manner. This allows the user to take into account all optical components from a single lens to the complex optical systems required to launch a Rayleigh laser guide star. To model the region of interest, point in space has been chosen, and to simulate the beacon, the range gate of 10 to 12 kilometers. Following this, the collection optics are considered and their efficiency values, to include reflectivity, transmission, and detection efficiency are input into the program. Once the simulation is run, there are several outputs of direct use to this study, including power in bucket (light which reaches the target altitude), total backscatter, C_N^2 values, and range parametrics which show the performance of the guide star as a function of altitude.

All of the following simulations were done as if they were at the JBO-Q observatory site, at 2300 with 50% humidity, moderate summer aerosols in a rural environment. There was a boundary layer introduced at 1000 meters, and the pressure at ground level was assumed to be 1000 bars, while the temperature is at 79° F. The ExPERT at the 2100-0000 hours EST timespan in summer was used for the atmosphere, with moderate summer levels of aerosols. The Bufton wind model was used. The first figure shows the HV 5/7 atmospheric profile which represents the turbulence in the following simulations. Recall that 10^{-13} is strong turbulence, while 10^{-15} can be considered moderate to weak turbulence.

Figure 4.2 (left) shows the C_N^2 altitude profile based on the HV 5/7 model in HEELEOS. Figure 4.2 (right) shows various atmospheric data as a function of altitude. These changing values are the primary factors which drive the C_N^2 values seen in Figure 4.1.

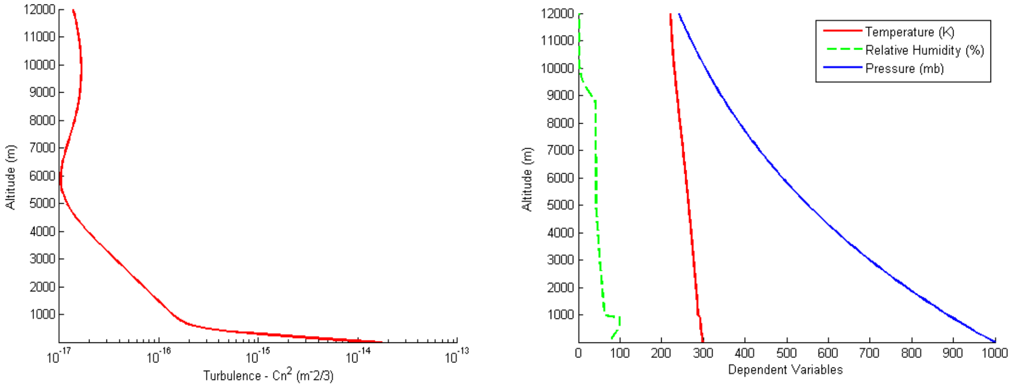

Figure 4.2 (left) C_N^2 profile generated as a result of the input parameters discussed applied to the HV 5/7 model. (right) Atmospheric data which feeds the results of the turbulent profile seen in Figure 4.1. Note the sharp drop in humidity after the boundary layer, and then another drop after 9000 meters.

IV.1.A 355 nm

The first simulation was done with the Questek 2580 Excimer Laser, which operates at 355 nm. Here we will see the highest backscatter results, as we would expect from the λ^{-4} relationship found in the Rayleigh backscatter formula. Incidentally, this laser was used at the University of Indiana for a study on laser guide star design. Subsequently, the guide star was put into functional use following the study. Due to the UV wavelength, this laser has the added benefit of circumventing FAA regulations as aircraft windows are opaque to 355 nm.

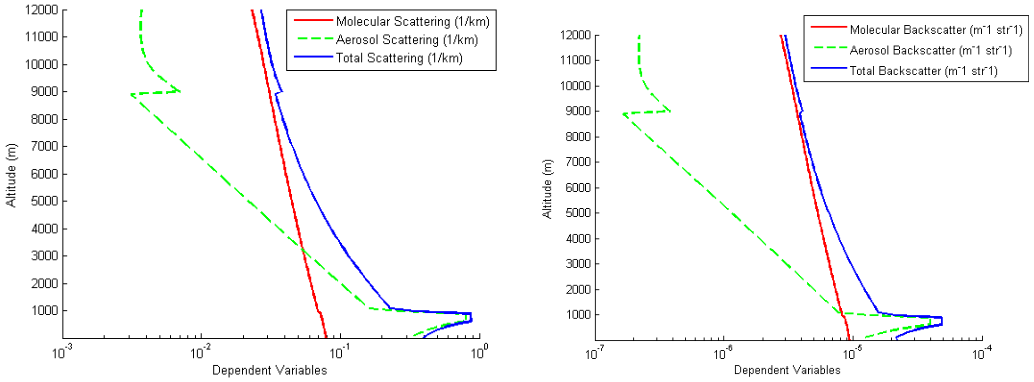

Figure 4.3: (left) The total scattering values for the 355nm Questek 2580 Excimer Laser across the entire scattering column. (right) The aggregate backscatter which is detected at the primary wavefront sensor and the collection optics as a function of altitude.

The sharp spikes in Figure 4.3 are to be expected at the two boundary layers as these contain increased amount of aerosol particles. These particles give an additional boost to the normal molecular scattering, even overtaking it until approximately 3500 m.

Figure 4.3 (right) shows the total backscatter as a result of the molecular and aerosol backscattering. These values are two to three orders of magnitude lower than the total backscatter as this is limited by the direction of the scattering, but this is the energy that is detected as the laser guide star.

IV.1.B 532 nm

Moving onto the 532 nm Matrix laser, we see that the scattering is slightly less efficient than the excimer laser, when compared to Figure 4.3.

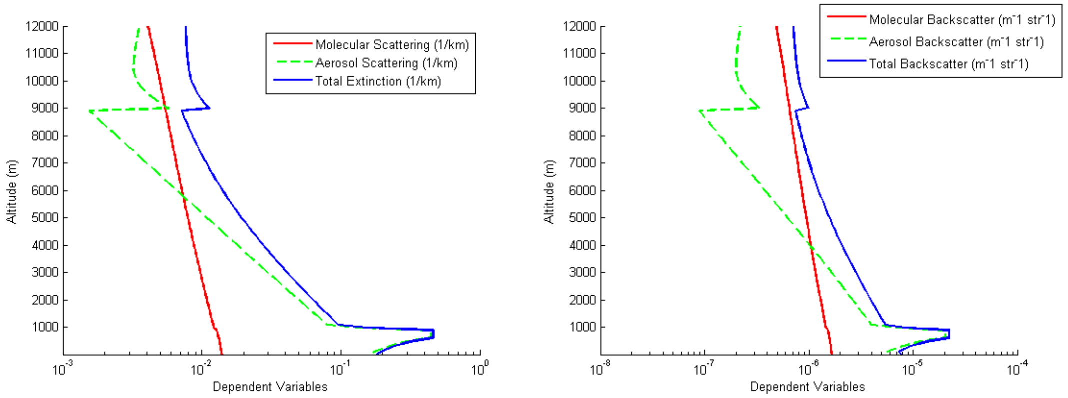

Figure 4.4: (left) The total scattering for the Matrix 532-14 laser in the same atmospheric conditions as the Excimer laser. (right) The total backscatter at the primary mirror of the 532 nm Matrix 532-14 laser.

The 532 nm laser was one of the most popular choices in the early development of Rayleigh laser guide stars as they were relatively cheap (in the tens of thousands of dollars) and dependable. Solid state green lasers had been in development for several decades as of the early 1990's, when laser guide stars were under development by non-Department of Defense scientists. Due to the sensitive nature of lasers aimed in space, the Department of Defense worked on this technology in secret for a number of years. Astronomers were quickly bringing the public domain up to the level of the Air Force. It is for this reason that the Department of Defense decided to declassify most of the work they had done on the topic [16].

.

IV.1.C 1064 nm

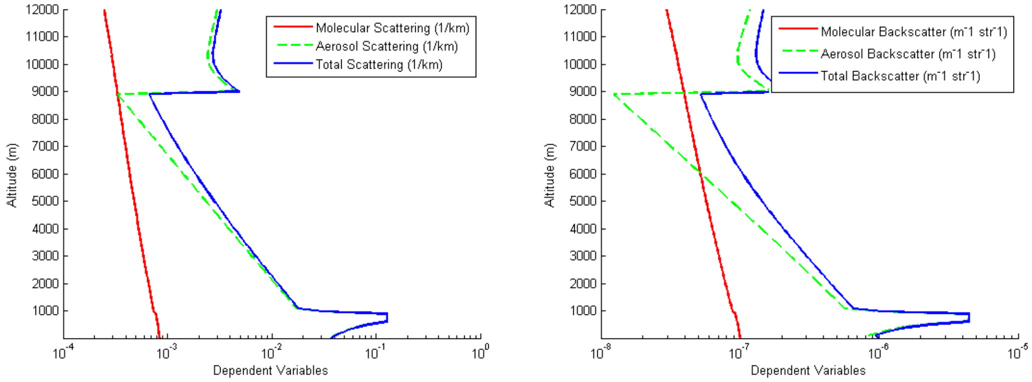

Figure 4.5: (left) The total scattering effects for the 1064 nm laser and (right) the total backscatter at the primary mirror for the 1064 nm laser.

Finally, the infrared 1064 nm Coherent laser is investigated. At this wavelength, aerosol scattering dominates molecular scattering, but we see an order of magnitude drop in the backscattering when compared to the visible and UV wavelengths. This is one of the chief reasons that IR wavelength guide stars are not used.

IV.1.D Tatarski Model

The next atmospheric model investigated in HELEEOS is the Tartarski model. The turbulent profile of the Tatarski model is as shown in Figure 4.6, and will be used to calculate the scattering returns of the three laser guide stars.

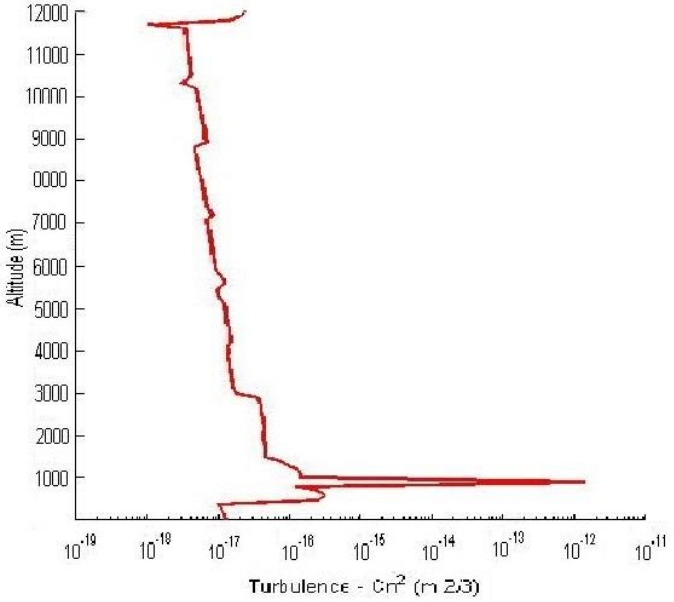

Figure 4.6: The Tatarski spectrum. In order to generate, the same atmospheric parameters as the HV 5/7 simulations were used.

The Tatarski spectrum is discussed in Chapter three, and is another atmospheric model used to predict the efficiency of atmospheric attenuation of optical propagation. First again, we investigate the 355 nm laser guide star.

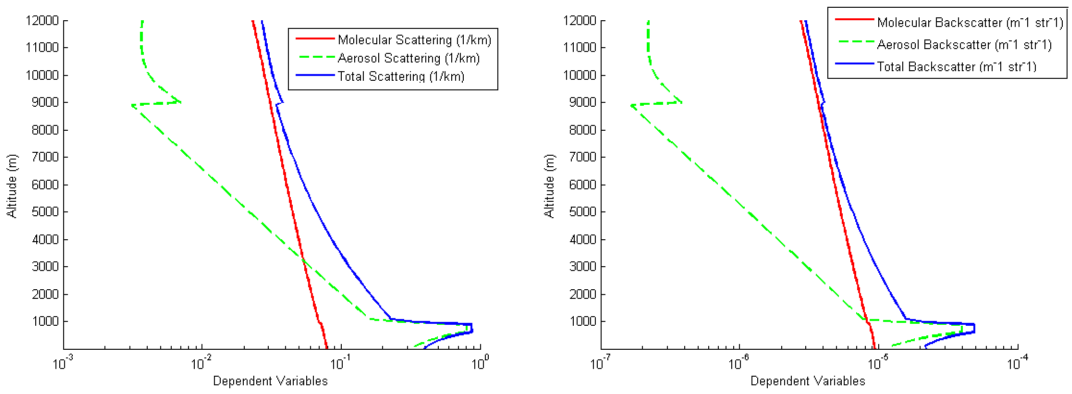

Figure 4.7: The total scattering (left) and total backscattering (right) values for the Tatarski model 355 nm laser.

The striking resemblance to the HV 5/7 model can be explained by the fact that while the Tatarski model seems to be more erratic than the HV 5/7 model, the C_N^2 values for the altitudes in question, 11 km, are quite similar, e.g, approximately 10^{-17}.

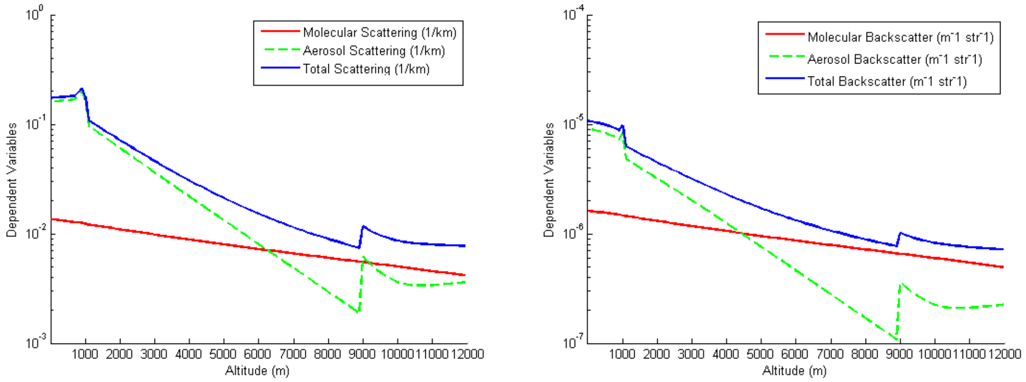

Figure 4.8: The total scattering (left) and total backscattering (right) values for the Tatarski model 532 nm laser.

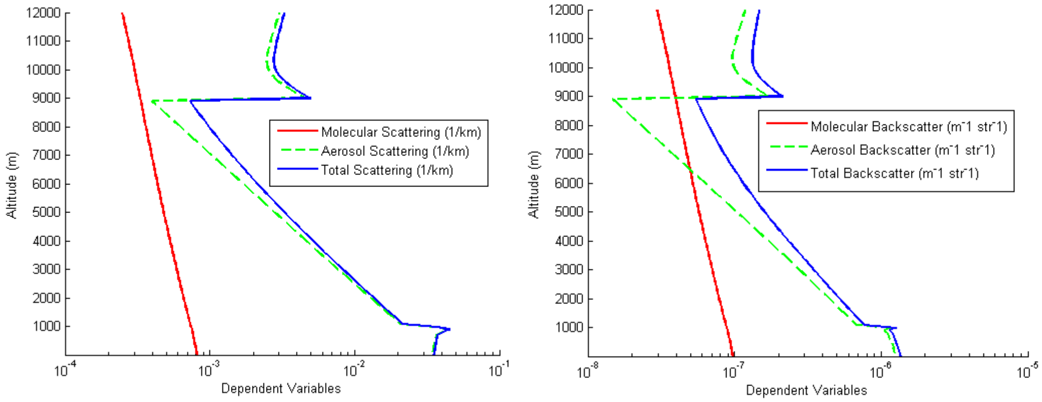

Figure 4.9: The total scattering (left) and total backscattering (right) values for the Tatarski model 1064 nm laser.

The last data products discussed will be the power on target, power backscattered to the detector, and the ratio of laser energy that is returned back to the detector.

The ‘Power on Target’ is the amount of laser light that reaches the central range gate depth. This is then modified by the backscattering coefficient to calculate the power returned to the detector.

Following this, the ratio of the laser power returned to the detector was calculated in order to determine the efficiency of the laser beacon created, as seen in figure 4.10.

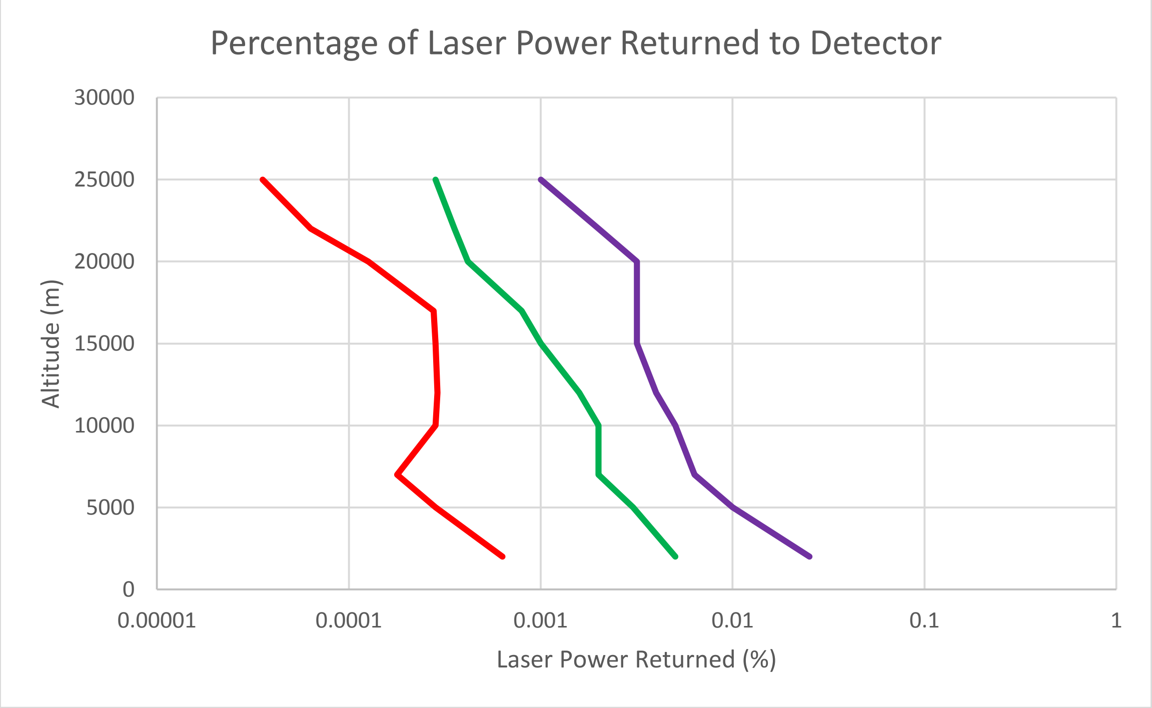

Figure 4.10: Laser power returned to the detector as a percentage of the initial laser power which leaves the laser launch telescope.

IV.2 Laser Environmental Effects Definition and Reference (LEEDR)

LEEDER, also developed at the Air Force Institute of Technology, allows for the more accurate and higher resolution modeling of the atmosphere and its effects on optical propagation. Permitting the high fidelity calculation of spectrum specific path transmittance, extinction, and attenuation, as well as the mean scattering affects over the entire atmosphere and backscattering in particular. It is also capable of calculating the power received by the observer as a result of the two way optical effects of atmospheric turbulence, integrating over the entire slant path.

Again, the three different wavelengths are used in order to compare and contrast the three proposed laser guide star systems. It is here that we will see stark differences between the visible, UV, and IR laser systems. The wavelength dependence on scattering, absorption, and transmittance is clear.

IV.2.A 355 nm

Path Transmittance	0.039
Path Extinction (1/km)	0.265
Path Specific Attenuation (dB/km)	1.15
Surface Visibility (km)	9.98
Slant Path Visibility (km)	32.8

Table 4.1: Path specific propagation variables.

Table 4.1 shows the total integrated values for specific variables over the entire optical path. These values represent the total aggregated effects of the atmosphere on the beam, as seen at the target of interest. The transmittance is the total beam power return seen by the observer. This is a result of the atmospheric scattering, absorption, and refraction and is an accurate representation of the total fluence detectable by the observer at the target altitude of 10 km.

Figure 4.11 gives a graphical representation of the scattering of a laser. This will assist readers in forming a physical picture of the properties being discussed.

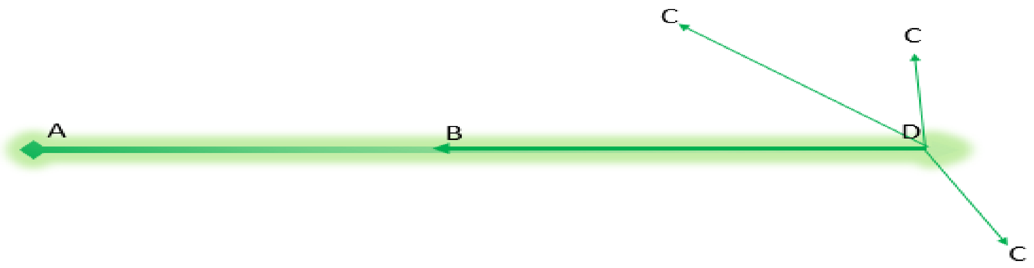

Figure 4.11. A graphical representation of some of the path specific propagation values. ‘A’ denotes the main beam as it exits the aperture, ‘B’ represents backscattering, ‘C’ is general scattering, and ‘D’ represents the aggregate effects of attenuation and extinction known as the total path transmittance at the final target distance (also called forward scattering). This defines how much energy reaches the target altitude.

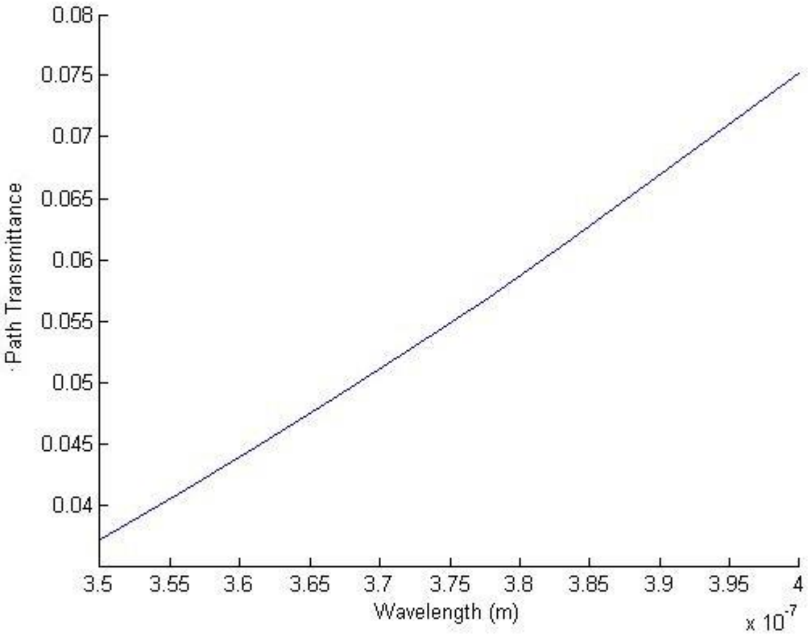

Figure 4.12: The total transmittance of the atmosphere as a function of wavelength. These values are calculated at the target altitude with a range gate of 10 to 12 km.

Figure 4.12 shows total path transmittance as a function of wavelength. Note that the current laser wavelength of 355 nm has a value of only approximately 0.04, This is due to the foggy nature of the atmosphere at ultraviolet wavelengths.

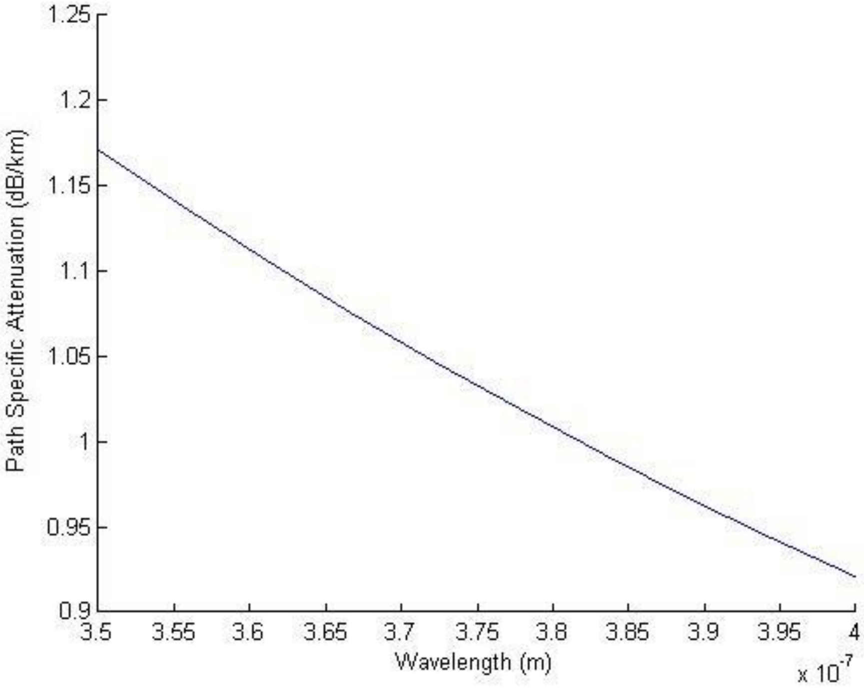

Figure 4.13: The path specific attenuation as a function of wavelength. These values are calculated at the target altitude with a range gate of 10 to 12 km.

Figure 4.13 shows the total path attenuation as a function of wavelength. The trend apparent here concurs with the path transmittance Figure, which shows an approximately opposite slope.

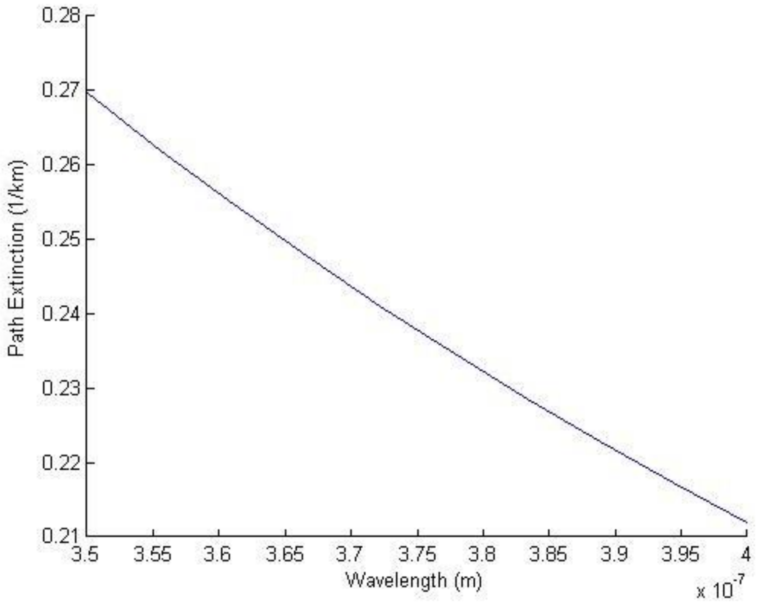

Figure 4.14: The path specific extinction as a function of wavelength. These values are calculated at the target altitude with a range gate of 10 to 12 km.

Figure 4.14 shows the extinction as it relates to wavelength. This concurs with both the attenuation and transmittance figures, and further shows the effects of the ‘foggy’ atmosphere with respect to the UV spectrum.

A quick pause to discuss the phase angle figure, depicted in figure 4.15. The scattering cross section is visualized as a function of a phase angle. The phase angle in this figure is the dependent variable of the phase function which describes the Rayleigh backscattering cross section. This helps show a spatial distribution of the backscattering cross section. Here, 0° is forward scattering and 180° is backscattering.

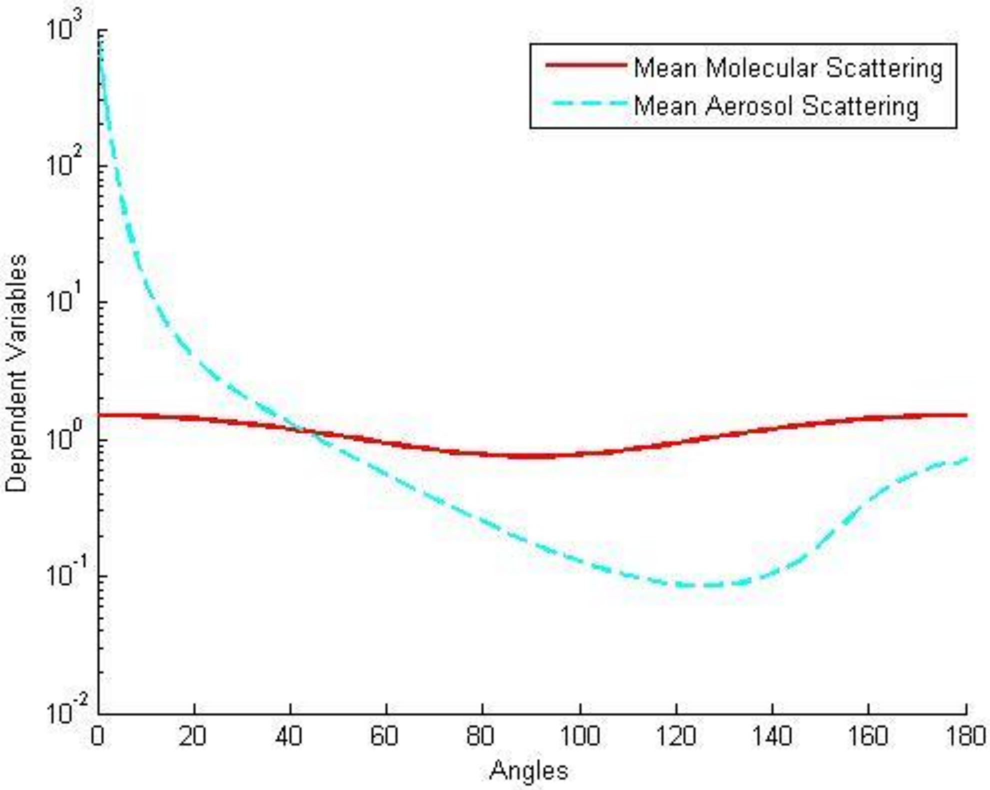

Figure 4.15: The mean scattering, both molecular and aerosol, as a function of phase angle. These values are calculated at the target altitude with a range gate of 10 to 12 km.

Figure 4.15 shows the mean (total) scattering as a function of phase angle with respect to the target volume. Note the angular dependence of aerosol scattering, while molecular scattering is relatively uniform. This scattering is due to the composition of the atmosphere more than any of these parameters, though pressure has the most effect as it is related to density, thus the number of scatterers.

IV.2.B: 532 nm

Path Transmittance	0.210761
Path Extinction (1/km)	0.127552
Path Attenuation (dB/km)	0.553951
Surface Visibility (km)	9.98
Slant Path Visibility (km)	32.76

Table 4.2: Path specific propagation variables.

Table 4.2 shows the same properties as table 4.1, but now for the 532 nm Coherent laser. The transmittance is higher than the UV by roughly an order of magnitude. This is due to the wavelength dependence mentioned in chapter two. The UV scatters much more than the visible light, thus attenuating the beam much more efficiently. The 532 nm light, therefore, travels more effectively through the slant path. For these purposes, a slant path can be defined as any path which deviates from a zenith path, which would be a normal angle from the surface of the Earth. However, one must take into account that these effects will also subtract from the total backscattering effect, which is the value used to create the artificial laser guide star.

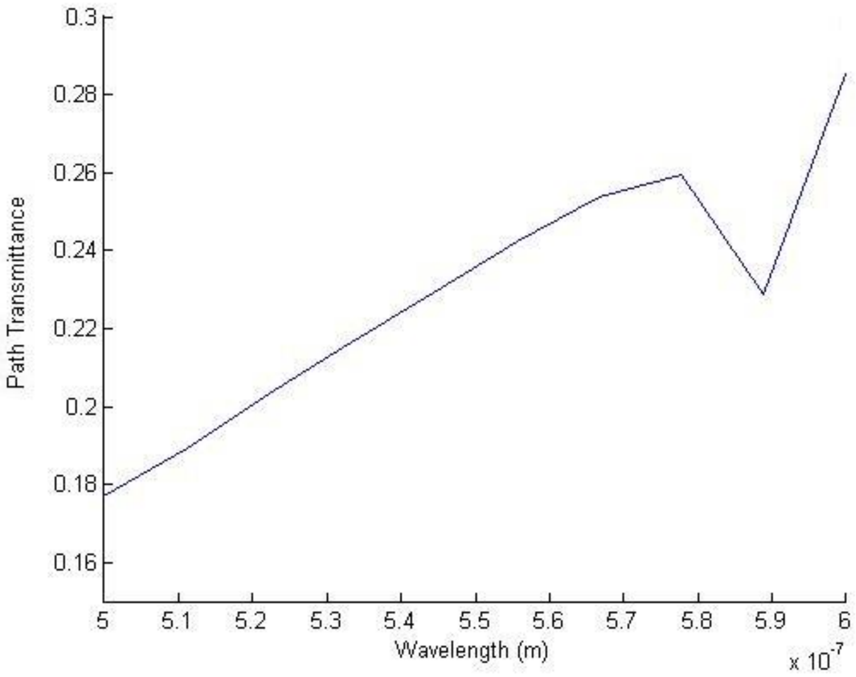

Figure 4.16: The path transmittance as a function of wavelength. These values are calculated at the target altitude with a range gate of 10 to 12 km.

The higher path transmittance seen in Figure 4.16 is advantageous to the JBO-Q laser guide star, as the limited budget restricts the brightness of lasers available at all wavelengths. As discussed before, 532 diode pumped solid state (DPSS) lasers are relatively affordable and dependable. The reduction of backscattering, which can be seen in both the HELEEOS and LEEDR simulations, is a trade-off parameter with the substantial increase in laser power which reaches the range gate.

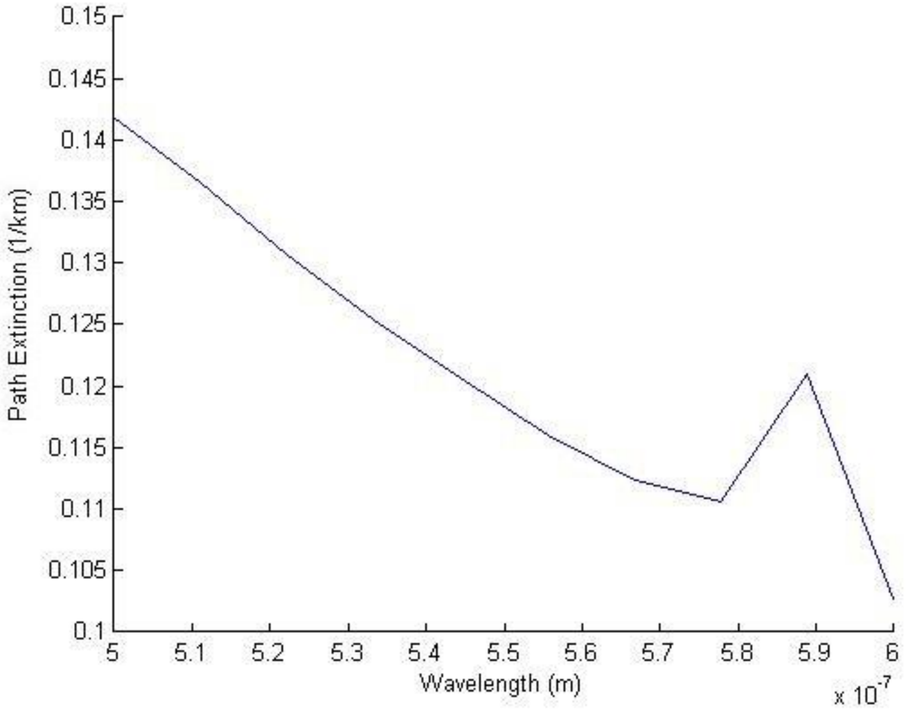

Figure 4.17: The spectrum specific path extinction of visible wavelengths. These values are calculated at the target altitude with a range gate of 10 to 12 km.

In Figure 4.17, the path extinction of visible wavelengths are shown. Here we see that the extinction is approximately half as much as in the UV wavelengths, and thus more advantageous for the purposes of a low budget laser guide star. Note the bump in extinction at approximated 589 nm, due to sodium. This must be taken into account when designing a sodium laser guide star. The transmittance also shows a 0.05 dip at the same wavelength. This fact, combined with the fact that sodium laser guide stars are designed to operate at much higher altitudes, sheds light on just how powerful the laser must be in order to produce an effective sodium laser guide star.

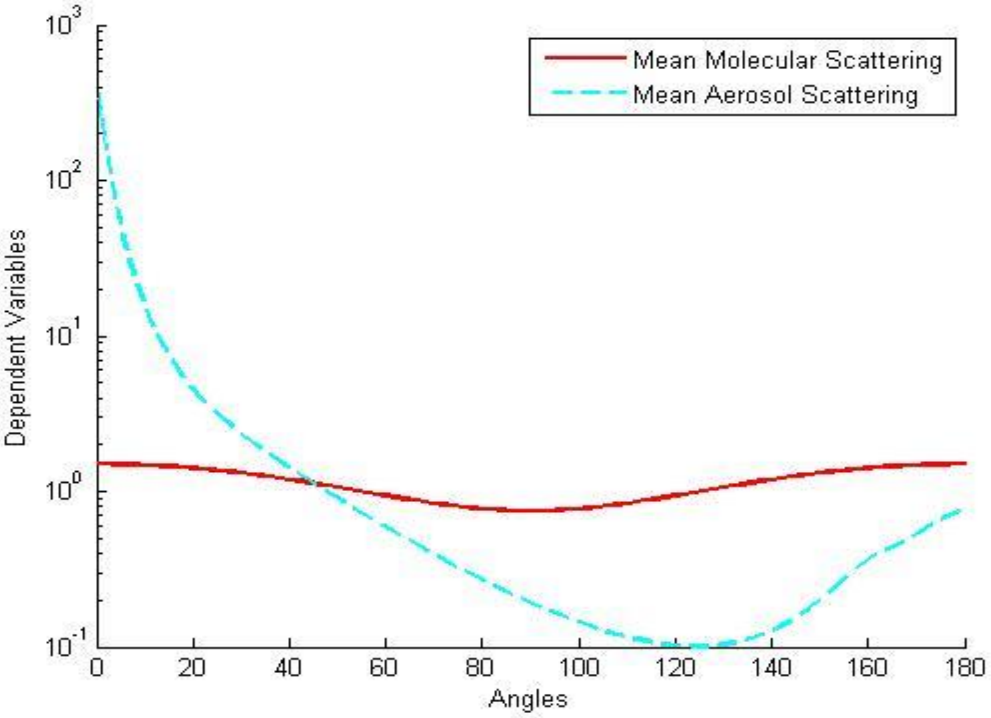

Figure 4.18: The mean scattering values as a function of phase angle. These values are calculated from the observers standpoint with a range gate of 10 to 12 km.

Figure 4.18 shows the scattering values of the 532 nm laser. For the purposes of a laser guide star, a good backscatter produces a more efficient scattering effect.

IV.2.C 1064 nm

Path Transmittance	0.660519
Path Extinction	0.0339747
Path Attenuation	0.14755
Surface Visibility	9.98
Slant Path Visibility	32.76

Table 4.3: Path specific propagation variables.

Moving on to the 1064 nm laser, we now see the clear disadvantage granted by the infrared. The path transmittance is substantially higher than both the UV and visible wavelengths because the scattering wavelength dependence comes heavily in to play. Here, most of the beam is allowed to transmit through the atmosphere and into space. Coincidentally, this is one of the main reasons that 1064 nm lasers are used in Satellite Laser Ranging (SLR), because it is here that researchers want the maximum light to reach their intended target.

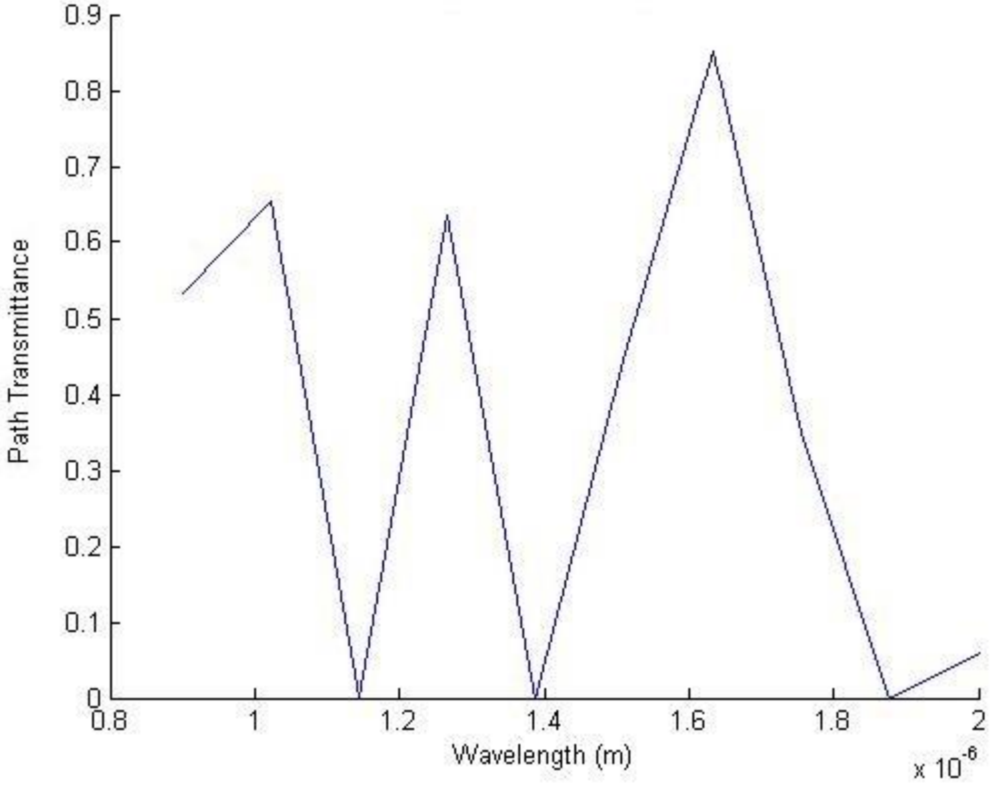

Figure 4.19: The path transmittance in the short wave infrared (SWIR). These values are calculated at the target altitude standpoint with a range gate of 10 to 12 km.

As can be seen in Figure 4.19, the path transmittance significantly in the shortwave infrared region around one micron. At the 1064 wavelength, however, the transmittance is still more than double the transmittance of the 532, and almost four times that of the 355 nm system.

Figures 4.19 and 4.21 also show the disadvantage of the IR system for use as a laser guide star. Since the laser light does not scatter nearly as efficiently as the visible and UV wavelengths, most of the laser energy travels through the atmosphere relatively uninhibited.

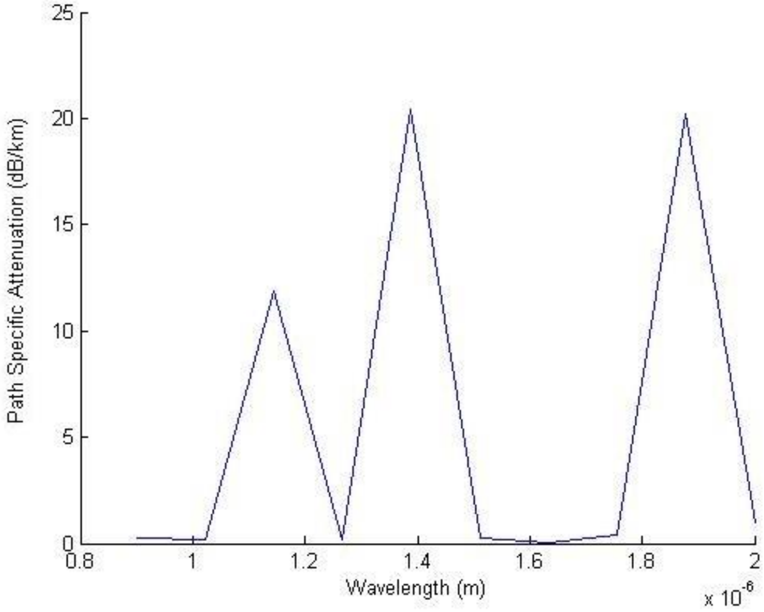

Figure 4.20: The spectrum specific path attenuation in the SWIR bandpass. These values are calculated at the target altitude with a range gate of 10 to 12 km.

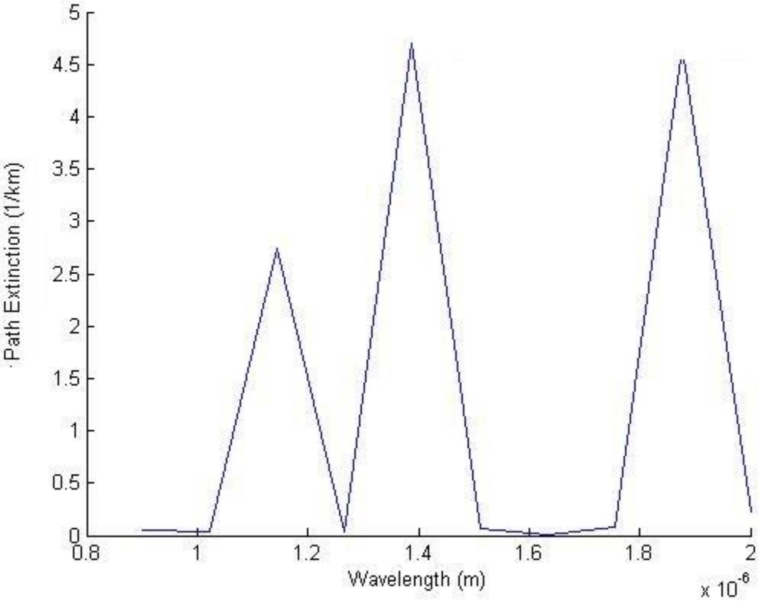

Figure 4.21: The path specific extinction of the SWIR bandpass along the slant path. These values are calculated at the target altitude with a range gate of 10 to 12 km.

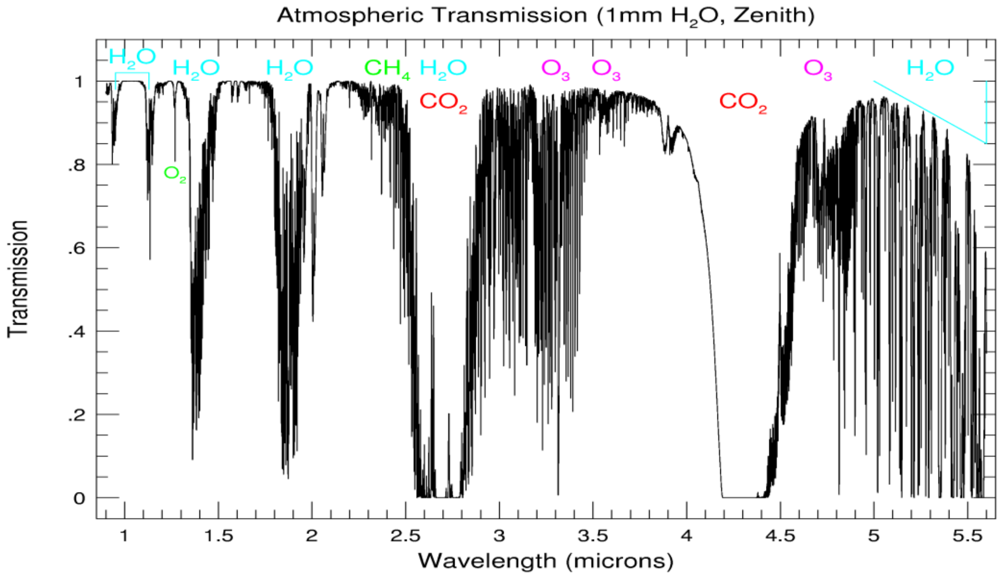

Figure 4.22: The atmospheric transmission spectrum in the SWIR to MWIR wavelengths [23].

For reference, the atmospheric transmission spectrum in the short wave IR, is shown in figure 4.22 [23].

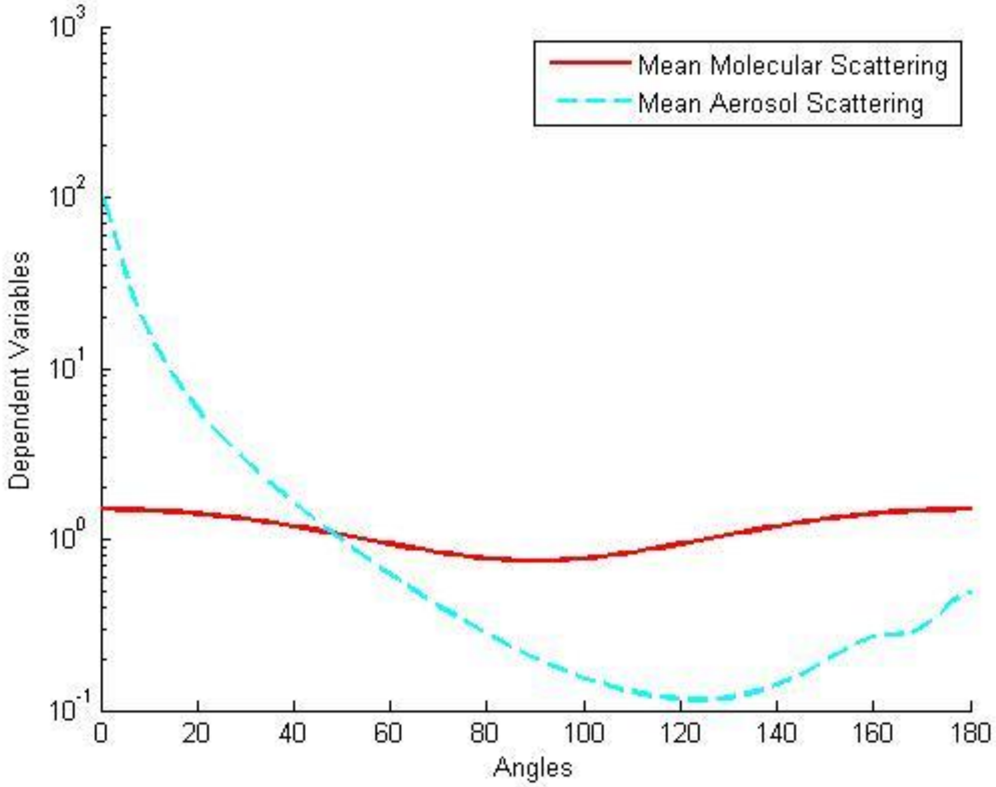

Figure 4.23: The total scattering effects in the SWIR as a function of angle. These values are calculated at the target altitude with a range gate of 10 to 12 km.

Since it is the backscattering effect which creates the laser guide star, figures 4.23, 4.18, and 4.15 can all be compared to determine the amount of total laser energy which is returned directly back to the telescope. All of the figures mentioned have a very small fraction of total laser energy returning (< 1%) at the backscattering angle of 180°, but there is still a significant loss when using the IR laser. The value for the IR laser is approximately one half of an order of magnitude less than for the UV laser.

IV.3 System Performance (Satellite Visualization and Signature Toolkit)

Based on the Thorlabs Wavefront Sensor described and chosen in Chapter III, a model was built in the Satellite Visualization and Signature Toolkit (SVST) in order to test its validity with the laser guide star system. Because the 532 nm Matrix laser is the most attractive candidate, it was chosen to be used in this model. Unfortunately, SVST is spectrally limited to Visible and IR wavelengths, so the UV case was unable to be modelled.

Figure 4.24 shows the spectral performance of the Thorlabs WFS. This includes not only the transmission of the collection optics, but also the spectral bandpass filter, and the quantum efficiency of the detector. Additionally, an approximate model of the atmospheric transmission is overlaid. All of these effects are totaled, and lead to the net end-to-end transmission of the laser light. This is the maximum percentage of total source light which falls on the detector plane. This source is the laser guide star which results from the chosen range gate. In order to create a laser guide star, the fluence magnitude must be greater than the minimum sensitivity of the sensor, and be above the noise floor.

For laser beacon applications, background noise is usually negligible. Detector read noise, or thermal noise, is the main factor contributing to the signal to noise ratio.

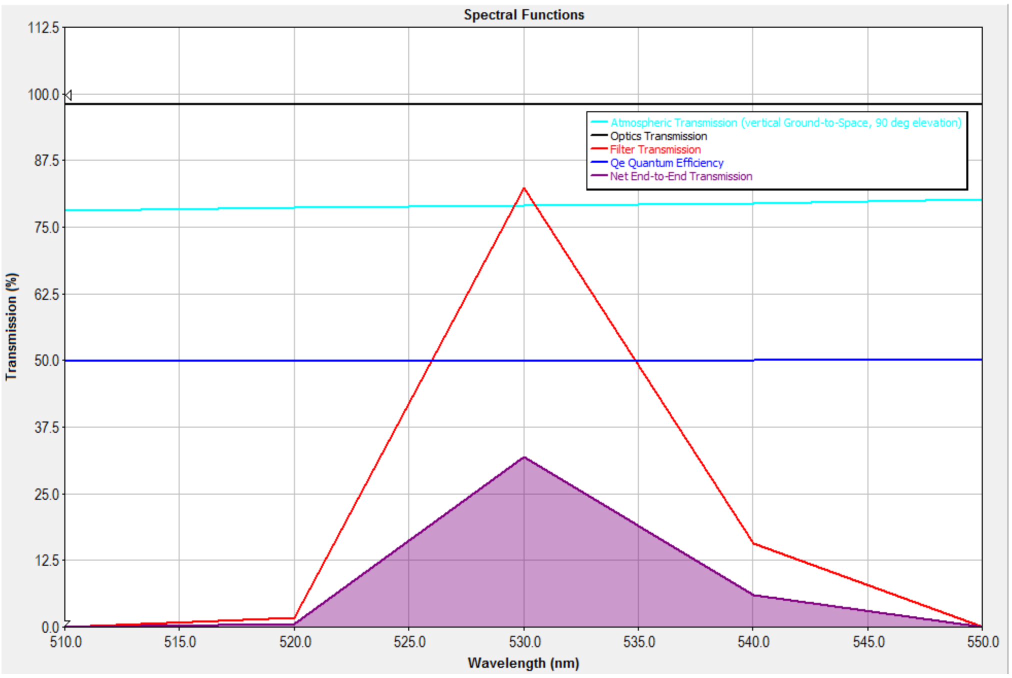

Figure 4.24: The total system throughput of the atmosphere and optics as seen by the Thorlabs Shack-Hartmann Wavefront Sensor in the visible spectrum.

This sensor, based on the backscatter Figures of the HELEEOS models, provides sufficient sensitivity for use in the JBO-Q laser guide star system when used in combination with the Matrix 532 nm laser. When placed in the proposed path, the Thorlabs Shack-Hartmann WFS yields a net efficiency of nearly 36 percent. This means that the system will detect approximately 36 percent of the light which reaches it from the range gate.

Here, the backscattered power that reaches the detector while using the Matrix-532 laser is approximately 10 milliwatts (down from 14 Watts) as found by the master lidar equation spreadsheet. This is collected by the 2.92 m^2 collection aperture, and focused on to the detector face. There are approximately 1.4E+14 photons per second of laser light entering the detector, as a result from 1,000 pulses. This means there are approximately 1.4E+11 photons per pulse that travel all the way back to the detector.

Given a very conservative read noise estimate of 50 electrons per pixel (nominal is approximately 14), our signal-to-noise ratio should be approximately 400,000:1. This was found via Hardy's signal-to-noise (SNR) equation [1]

$$SNR = \frac{n}{(n \quad + me^2)^{1/2}} \tag{53}$$

Where here, n_c is the number of photons collected as found in the LIDAR equation, *m* is the number of pixels per subaperture, and *e* is number of read noise the electrons per pixel. To reach a SNR of 4, approximately 4000 photons are needed.

V. Results and Future Work

V.1 Results

Based on the simulations shown in chapter IV, an infrared laser would provide the least benefits as a Rayleigh laser guide star at JBO-Q. The minimal scattering effect of the atmosphere in the IR bandpass is simply insufficient for the purpose of artificial guide star generation. Both the UV and visible systems, however, show promise.

Due to the highly efficient scattering effect that the atmosphere has on the 355 nm laser light, the Excimer laser creates an extremely effective laser guide star. Unfortunately, due to the low demand that astronomy has on the laser manufacturing market, there was simply not enough demand to keep making high energy UV lasers with laser guide star parameters. The main market for these lasers is for use in laser eye surgery. The compounded effect of the primary laser beam scattering and absorption, along with the scattering and absorption of the backscattered photons traveling back towards the wavefront sensor, create a need for a high power laser that is simply outside of the budget constraints of a small project like the JBO-Q.

The visible wavelength Rayleigh laser guide stars paved the way for adaptive optics technology, and this was in part because of their effectiveness and affordability. The performance is comparable to that of the 355 nm system, and is an order of magnitude cheaper in upfront cost. The Excimer lasers are also gas based, requiring a high maintenance schedule and much more careful operation. Ease of operation is increased greatly by using DPSS lasers, and it also allows for more dynamic changes on the fly for use in other potential future experiments that cannot be foreseen when designing the current system. The efficient scattering, cost benefit, and easy setup and operation of the system make the 532 nm Matrix Laser the optimum choice for the JBO-Q Rayleigh Laser Guide Star. It is the recommendation of this paper to move forward with the equipment chosen and described in chapter three.

V.2 Future Work

Based on the success of the physical implementation of the proposed laser guide star, there are several experiments which could be performed.

Dynamic range gating could be used in order to generate an accurate, real time turbulent profile of the atmosphere above John Bryan State Park. This can be accomplished by changing the range gate in real time in order to collect returning photons from different altitudes. Using these photon return values, the observer can calculate the C_N^2 values and thus the turbulent profile of the atmosphere based on the derivations given in chapter II.

The addition of adaptive optics to the JBO-Q would greatly assist in its primary mission of space situational awareness (SSA) research and development. The SSA benefits would allow greater precision in target acquisition for tracking purposes, as well as increased data resolution for asset characterization. Furthermore, additional imaging research could allow a comparison of adaptive optics to other image compensation techniques which are in use today. While only a few more components are needed in order to accomplish this task, the integration into the JBO-Q would be more complex due to its unique design and lack of capacity for a Coudé path. While it is outside the scope of this paper, there is high confidence that such a system could be conceived and carried out.

A sodium guide star would be an alternative addition to the JBO-Q, but it would quite possibly be limited to only the use for adaptive optics, while much more effective for this purpose than Rayleigh guide stars. The guide star formation is limited to the sodium layer, above the atmospheric boundary layer of most common turbulence physics. In addition, the sodium guide star would be unable to be dynamically range gated as the lasers used for them are continuous wave (CW). This means that range gating in the traditional sense is impossible as the observer cannot distinguish which part of the beam backscatter is returning to their sensor.

The possibility remains that the Rayleigh laser guide star system could be kept intact after the installation of a sodium guide star, allowing for the changing of lasers in the injection system. This has been considered in the design concept of the Rayleigh laser guide star, and is another reason why the fiber optic injection system has been proposed. By keeping all of the injection optics physically separate from the laser sources, they can be moved with relative ease in order to facilitate the swapping of lasers into the launch telescope. After switching the lasers, it is only a matter of changing the scripts guiding the wavefront sensor in order to initiate the next guide star system.

In conclusion, this thesis has analyzed the possible options for installing a Rayleigh laser beacon for the atmospheric turbulence research which will take place at the John Bryan State Park Observatory Quad Axis Telescope. Due to the simulation work shown in chapter IV, it is the recommendation of the author to proceed with the final proposed equipment, with the confidence that the information given in this paper in combination with laboratory experimental configurations done for risk reduction experiments.

Bibliography

[1] Hardy, J. (1998). Adaptive Optics for Astronomical Telescopes. New York, New York: Oxford University Press.

[2] Newton, I. (2003). Opticks. Amherst, N.Y.: Prometheus Books.

[3] Platt, B., & Shack, R. (2001). History and Principles of Shack-Hartmann Wavefront Sensing. Journal of Refractive Surgery, 17, S573-S577.

[4] Minkin, Daniel, “A Simplified Method for Measuring Wavefront Tilt in an Optical Vortex,” November 2007, Locust Valley, NY. (Paper by a student of the Laser Teaching Center at Stony Brook University)

[5] Richardson, Louis Fry (2007). Weather Prediction by Numerical Process, Second Edition. Cambridge, United Kingdom: Cambridge University Press.

[6] Tennekes, Henk (1972). A First Course in Turbulence. Boston, Massachusetts: MIT Press Design Department.

[7] Fluids and Flow. (2015). Retrieved from http://www.spiraxsarco.com/Resources/Pages/Steam-Engineering-Tutorials/flowmetering/fluids-and-flow.aspx#close

[8] Pope, S. B., (2003). Turbulent Flows. Cambridge, United Kingdom: Cambridge University Press.

[9] George, William K (2013). Lectures in Turbulence for the 21st Century. Imperial College of London, London, United Kingdom.

[10] Owens, J. (1967). Optical Refractive Index of Air: Dependence on Pressure, Temperature and Composition. *Applied Optics, 6*(1), 51-59.

[11] Tunick, Arnold; Tikhonov, Nikolay; Voronstov, Mikhail; Carhart, Gary (2005). Characterization of Optical Turbulence (Cn2) Data Measured at the ARL A_LOT Facility. Adelphi, Maryland: United States Army Research Laboratory.

[12] Maccioni and Dainty (1997). Measurement of Thermally Induced Optical Turbulence in a Water Cell. *Journal of Modern Optics, 44*(6), 1111-1126.

[13] Andrews, Larry C; Phillips, Ronald L. Laser Beam Propagation Through Random Media, Second Edition. Bellingham, Washington: SPIE – The International Society for Optical Engineering.

[14] How a Shack-Hartmann Wavefront Sensor Works. Retrieved from http://www.thorlabs.com/newgrouppage9.cfm?objectgroup_id=5287

[15] Loktev, Vdovin, Klimov, Kotova, Naumov (2005). Modal Wavefront Correction with Liquid Crystals: Different Options. *Proceedings of SPIE, 5741,* 163-170.

[16] Thompson, Laird A; Teare, Scott W (2002). Rayleigh Laser Guide Star Systems: Application to the University of Seeing Improvement System. *Publications of the Astronomical Society of The Pacific, 114,* 1029-1042.

[17] Kissell, Kenneth E (1965). Advantages of A 4-Axis Tracking Mount for the Photoelectric Photometry of Space Vehicles. USAF Aerospace Research Laboratories: Wright-Patterson Air Force Base, Ohio.

[18] Hecht, Eugene (2008). Optics. Essex, United Kingdom: Pearson Education Limited.

[19] Litron Technical Note. True TEM00 or Not? Retrieved from http://www.litronlasers.com/pdf%20files/LTN%20True%20TEM00_0112_1.pdf

[20] Stephens, Johnson, and Languirand (1990). Beam Path Conditioning for High-Power Laser Systems. *The Lincoln Laboratory Journal,3 (2)*, 225-244.

[21] Laser Induced Damage in Optical Fibers. Retrieved from https://www.thorlabs.com/newgrouppage9.cfm?objectgroup_id=1596

[22] Yutaka et al. (2006). The Laser Guide Star Facility for Subaru Telescope. *Proceedings of SPIE, 6272(47)*, 627247-1 – 627247-7

[23] Lecture 29: The Earth's Atmosphere. Retrieved from http://www.astronomy.ohio-state.edu/~pogge/Ast161/Unit5/atmos.html

[24] P. Madec (2015). Overview of Deformable Mirror Technologies for Adaptive Optics. Imaging and Applied Optics, OSA Technical Digest (online), paper AOTh2C.1.

[25] Phase angle representations. Retrieved from http://www.electronics-tutorials.ws/accircuits/acp25.gif?81223b

Appendix:

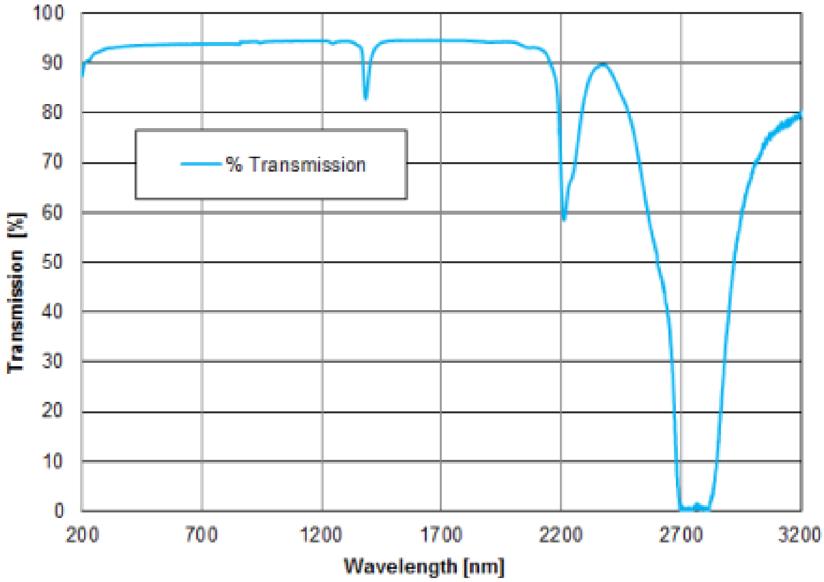

Figure A.1: The wavelength dependent transmission values of fused silica.

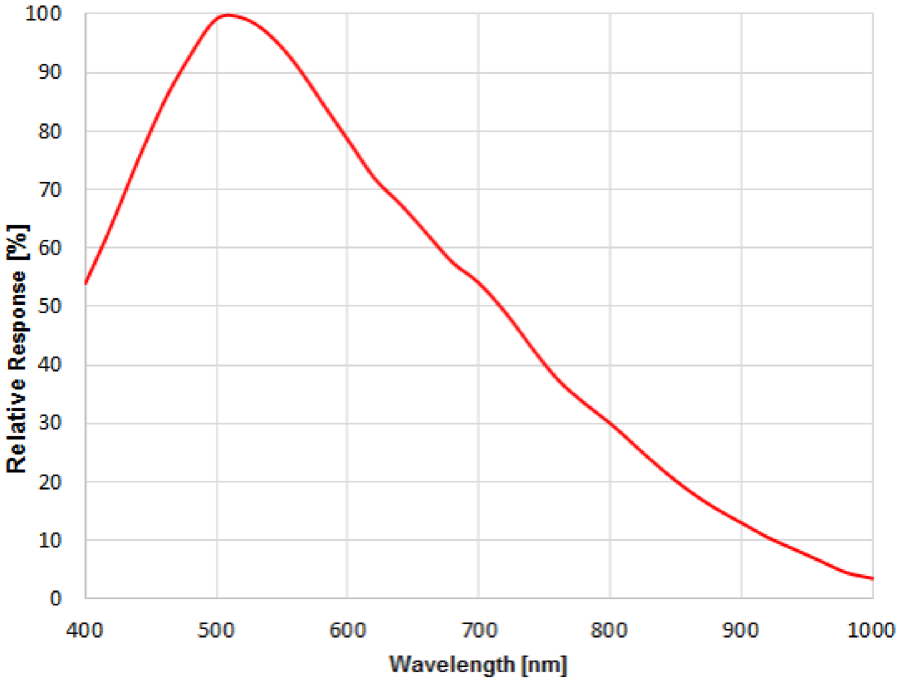

Figure A.2: The relative responsivity of the Thorlabs Shack Hartmann Wavefront sensor.

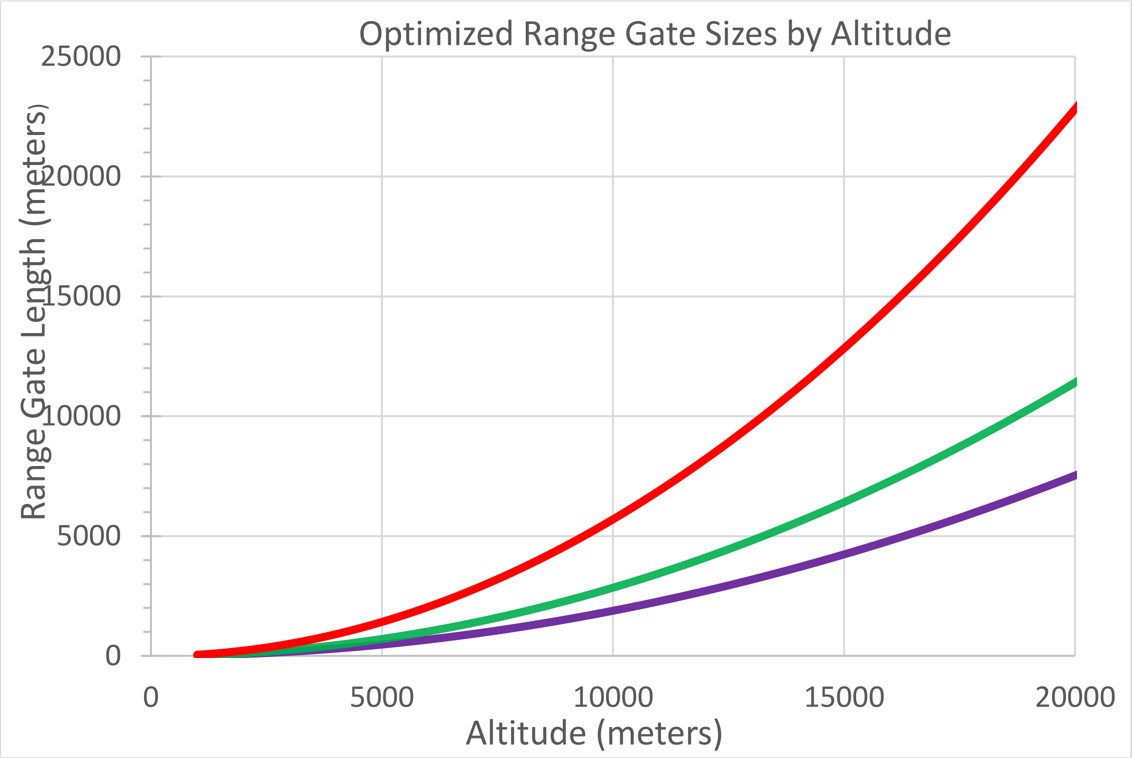

Figure A.3: Optimized range gate lengths for each wavelength. Red is the 1064 nm laser, green is the 532 nm laser, and purple is the 351 nm laser.

Laser	Pulse Width (ns)	Rep Rate (Hz)	Avg Power (W)	Divergence (rad)	Beam Size (m)	Final Laser Launch Diameter (m)	Final Divergence (rad)	Beam Quality After Injection Optics
Questek 2580	20	333	30	0.003	0.000198	0.1016	5.84646E-06	2.22441E-06
Matrix 532	20	1000	14	0.0042	0.00023	0.1016	9.50787E-06	3.33348E-06
VGEN-QS	125	1000	30	0.000045	0.0075	0.1016	3.32185E-06	6.66696E-06

Table A.1: Laser parameter specifications, taken from manufacturer data sheets.

Optical Property	Value
Attenuation at 532 nm	< 20 dB/km
Attenuation at 632 nm	< 10 dB/km
Attenuation at 1064 nm	< 5 dB/km
Single Mode cut-off wavelength	None

Table A.2: Optical properties of the Endlessly Single Mode Photonic Crystal Fiber chosen.

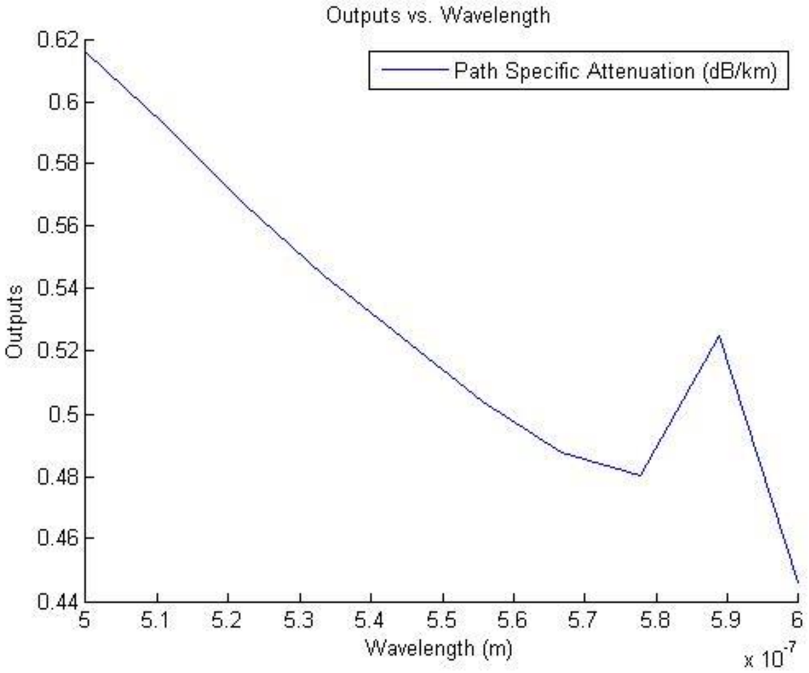

Figure A.4: The spectrum specific path attenuation as it relates to visible wavelengths.

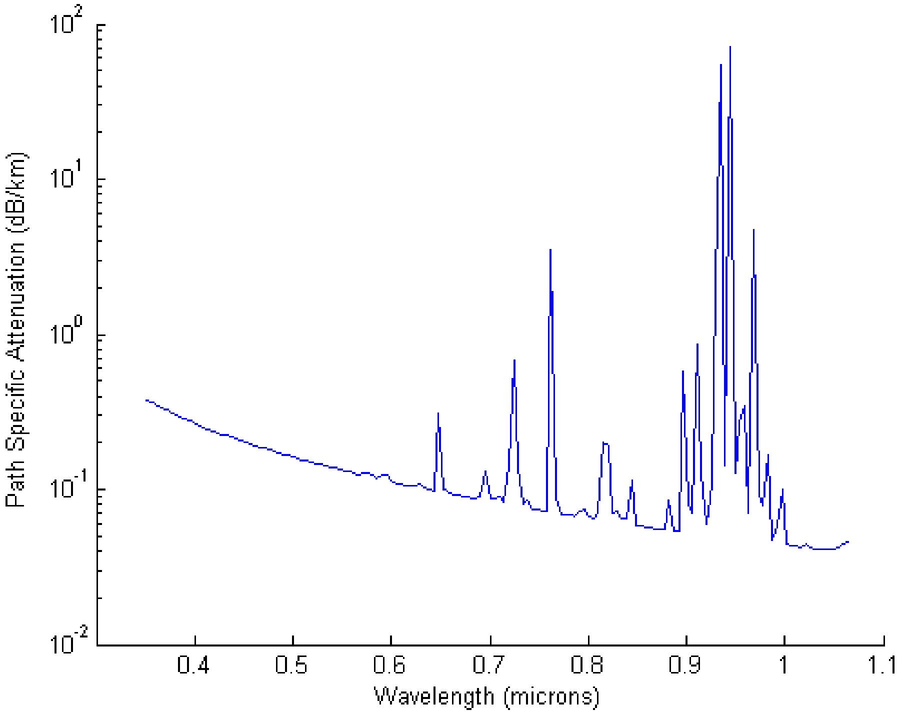

Figure A.5: The atmospheric attenuation of the bandpass of interest.

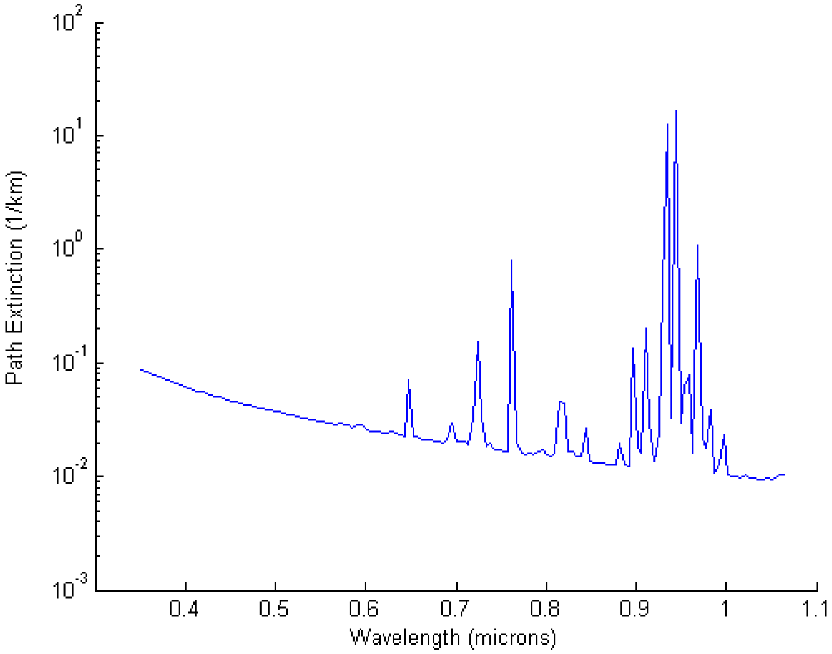

Figure A.6: The atmospheric extinction of the bandpass of interest.

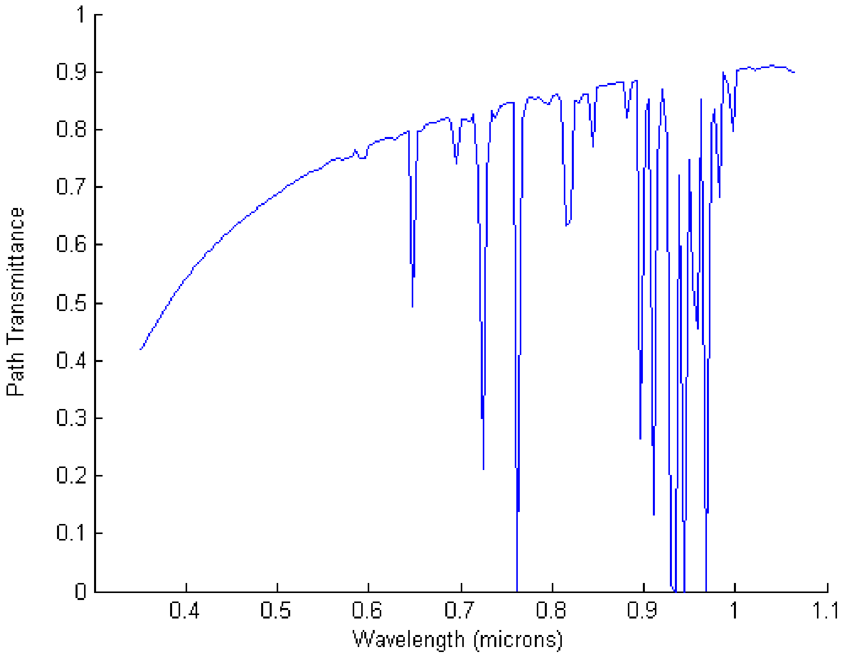

Figure A.7: The atmospheric transmittance of the bandpass of interest.

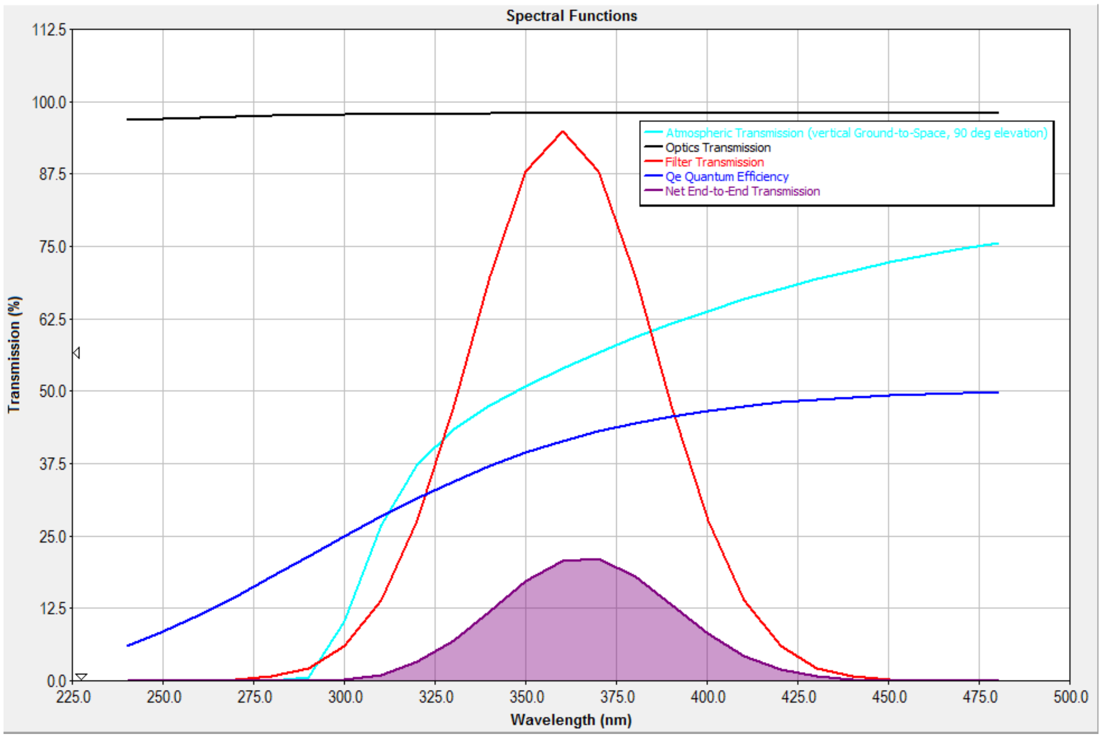

Figure A.8: The total system throughput of the atmosphere and optics as seen by the Thorlabs Shack-Hartmann Wavefront Sensor in the UV spectrum.

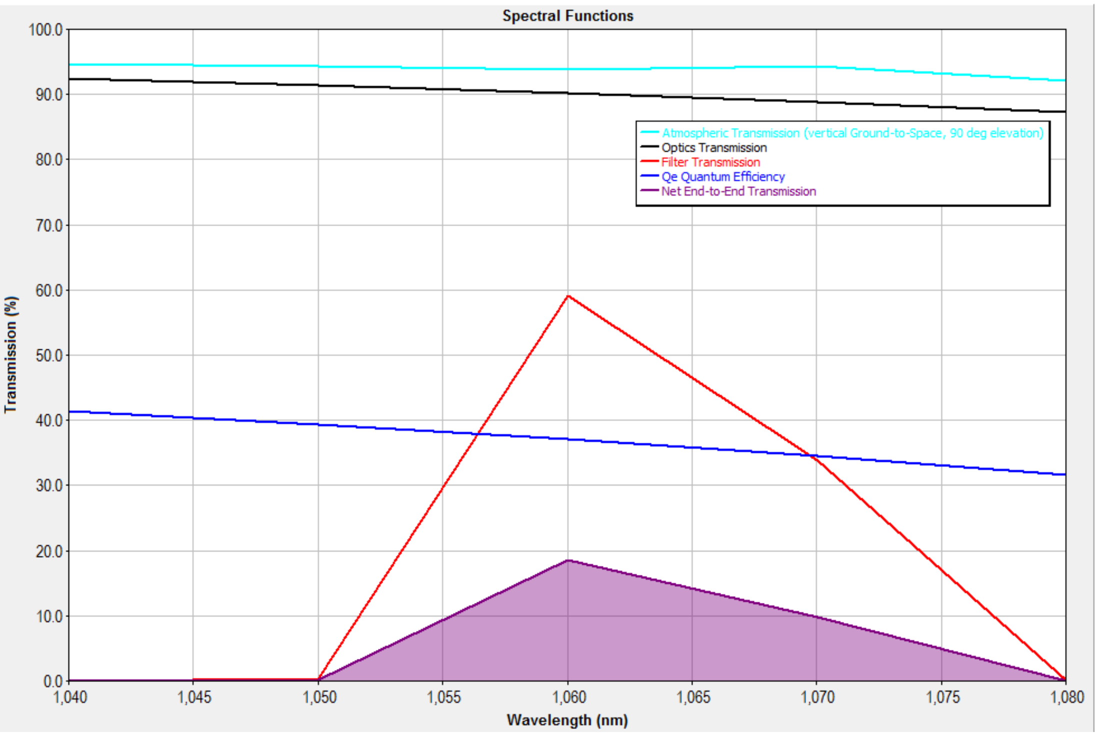

Figure A.9: The total system throughput of the atmosphere and optics as seen by the Thorlabs Shack-Hartmann Wavefront Sensor in the IR spectrum.